Final report

Numerical investigation on the failure mechanisms of particulate composite material under a various loading conditions using a damage constitutive model

P.I.: Hiroshi Okada, Ph.D., Associate Professor

Address: Department of Nano Structure and Advanced Materials
Graduate School of Science and Engineering, Kagoshima University
1-21-40 Korimoto, Kagoshima 890-0065, Japan

Telephone, Facsimile: +81-99-285-8249, +81-99-250-3181
E-mail: okada@mech.kagoshima-u.ac.jp

Report Documentation Page

Form Approved
OMB No. 0704-0188

1. REPORT DATE	2. REPORT TYPE	3. DATES COVERED
01 SEP 2006	**Final Report (Technical)**	**15-04-2004 to 21-08-2006**

4. TITLE AND SUBTITLE
Numerical investigation on the failure mechanisms of particulate composite materials under various loading conditions using damage constitutive model

5a. CONTRACT NUMBER
FA520904P0271

5b. GRANT NUMBER

5c. PROGRAM ELEMENT NUMBER

6. AUTHOR(S)
Hiroshi Okada

5d. PROJECT NUMBER

5e. TASK NUMBER

5f. WORK UNIT NUMBER

7. PERFORMING ORGANIZATION NAME(S) AND ADDRESS(ES)
Kagoshima University,1-21-40 Korimoto,Kagoshima 890-0065,Japan,JP,890-0065

8. PERFORMING ORGANIZATION REPORT NUMBER

9. SPONSORING/MONITORING AGENCY NAME(S) AND ADDRESS(ES)
The US Resarch Labolatory, AOARD/AFOSR, Unit 45002, APO, AP, 96337-5002

10. SPONSOR/MONITOR'S ACRONYM(S)
AOARD/AFOSR

11. SPONSOR/MONITOR'S REPORT NUMBER(S)
AOARD-044039

12. DISTRIBUTION/AVAILABILITY STATEMENT
Approved for public release; distribution unlimited

13. SUPPLEMENTARY NOTES

14. ABSTRACT
During the present research, the followings have been accomplished 1) The separate dilatational/deviatoric damage constitutive model was proposed along with a method to extract its material parameters from one-dimensional stress-strain curve. The damage model was implemented in the s-FEM computer program. 2) S-FEM formulation with the cohesive zone model has been proposed and has been implemented in the s-FEM program. 3) S-FEM analyses on particulate composite materials, with assuming the matrix damage and dewetting between the particles and matrix material, has been carried out. Some characteristic behavior of damages in the particulate composite materials has been revealed.

15. SUBJECT TERMS
Composite Fracture Mechanics, Numerical Simulation

16. SECURITY CLASSIFICATION OF:			17. LIMITATION OF ABSTRACT	18. NUMBER OF PAGES	19a. NAME OF RESPONSIBLE PERSON
a. REPORT	b. ABSTRACT	c. THIS PAGE			
unclassified	**unclassified**	**unclassified**		**77**	

Contents

Summary

In this research, the s-version finite element method (s-FEM) is used to carry out analyses on the particulate composite materials undergoing progressive damage. Matrix material is assumed to be a polymeric material. Hard particles are embedded in matrix material. S-FEM simplifies the modeling procedures for particulate composite materials because it allows us to build finite element models for the structure as whole and for particles and their vicinities, separately. They are called “global” and “local” finite element models. When particulate composite materials are modeled, the local finite element model contains a particle and its immediate surrounding region. The local finite element models are superposed on the global model. By adopting the s-FEM, placing particles in matrix material became a trivial task.

Matrix is considered to suffer from a material damage due to the growth and nucleation of microvoids. Also, the composite experiences damage due to particle-matrix dewetting. The former is accounted for by the use of a continuum damage constitutive law. The later is by a cohesive zone model. Two kinds of continuum damage models are used in this research. They are an isotropic and a separate dilatational/deviatoric damage constitutive law that accounts for the influences of hydrostatic and deviatoric stresses separately. The constitutive and the cohesive zone models were implemented in the s-FEM computer program.

Numerical analyses were carried out to reveal the characteristic deformation behavior of particulate composite such as the influences of hard particles to matrix damage, the influences of particle-matrix dewetting to matrix damage, etc.

The results revealed that the separate dilatational/deviatoric damage constitutive model with a small contribution from the deviatoric stresses was the most appropriate model among the models which were tested in this study. When the cohesive zone model is assumed at the interface between the particles and matrix material, the strength of bond of the cohesive zone determines the damage mode that dominates the other. When the bond is strong, the matrix damage is the major damage mode. When the bond is weak, the dewetting is the major damage mode.

The outcomes of present research revealed some characteristic behavior of progressive damage in polymeric particulate composites.

1. S-version Finite Element Method (S-FEM) for the analysis of particulate composite materials

1.1 Equation Formulations

In this section, we discuss about general formulations of the s-version finite element method (s-FEM). It is assumed that particles or fibers are distributed in the domain of analysis as shown in Figure 1. Though Figure 1 implies that the particles or voids are spherical in their shapes, there is no such restrictions in the mathematical formulation. The second phase material can be fibrous or any others in their shapes. Though the previous formulations of the s-FEM (see Fish [1] for example) assumes only one overlaid model to be superposed on the global model, we allow any numbers of finite element models to be superposed. Then, the overlaid models are allowed to overlap each other, as depicted in Figure 2. When the shapes of the embedded second phase materials are the same or similar to each other, the same local finite element model can be used repeatedly. Therefore, generating a model for the composite would be a simple task.

In the following discussions, the regions of the global and the *p*-th (*p*=1,2,3, ···, *M*) local finite element models are designated to be Ω^G and Ω^{Lp}, as depicted in Figure 3. We assume that there are a total of *M* local model regions. The displacements are defined based on the shape functions of elements in the global and local models, independently [see references such as Bathe [2] and Hughes [3] for the shape functions of finite elements]. We write them to be $u_i^G = u_i^G(\boldsymbol{x})$ in Ω^G and $u_i^{Lp} = u_i^{Lp}(\boldsymbol{x})$ in Ω^{Lp}, where $\boldsymbol{x}$ denotes the position of a material point. At a point which is not inside of any local model regions, the displacements u_i are the same as the displacement functions u_i^G of Ω^G.

$$u_i = u_i^G(\boldsymbol{x}) \tag{1}$$

At a point where some local finite element models overlap, the displacement functions u_i are given by the sum of displacement functions of the overlapped models. For example, at a point where the local models Ω^{Lp} and Ω^{Lq} $(1 \le p, q \le M,\ p \ne q)$ overlap on the global model Ω^G, the displacements u_i are represented by the sum of their

displacement functions, as:

$$u_i = u_i^G(\boldsymbol{x}) + u_i^{Lp}(\boldsymbol{x}) + u_i^{Lq}(\boldsymbol{x}) \tag{2}$$

To assure the continuities of displacements, those based on a local finite element model are set to be zero at its outer boundary. We let:

$$u_i^{Lp} = 0 \quad \text{at} \quad \partial\Omega^{Lp} \tag{3}$$

where $\partial\Omega^{Lp}$ designates the outer boundary of local model region Ω^{Lp}.
Stresses at a point are written in terms of strains through Hooke's law [see Sokolnikoff [4], for example].

$$\sigma_{ij} = E_{ijk\ell}\,\varepsilon_{k\ell} \tag{4}$$

where the elastic constants $E_{ijk\ell}$ may vary within the solid and are the functions of location of a material point.

$$E_{ijk\ell} = E_{ijk\ell}(\boldsymbol{x}) \tag{5}$$

The statement of principle of virtual work is written to be:

$$\int_{\Omega^G} \frac{\partial \delta u_i}{\partial x_j} E_{ijk\ell} \frac{\partial u_k}{\partial x_\ell} \mathrm{d}\Omega^G = \int_{\Omega^G} \delta u_i b_i \mathrm{d}\Omega^G + \int_{\partial\Omega_t^G} \delta u_i \bar{t}_i d\left(\partial\Omega_t^G\right) \tag{6}$$

where δu_i are the variations of displacements, b_i are the body force per unit volume, $\bar{t}_i$ are the prescribed traction vector on the traction prescribed boundary $\partial\Omega_t^G$. The variations of displacements δu_i are assumed in the same manner as the displacements

u_i, by the superposition at material points where they overlap. Thus, δu_i are written to be $\delta u_i = \delta u_i^G(\boldsymbol{x})$ where no local models overlap on the global model and $\delta u_i = \delta u_i^G(\boldsymbol{x}) + \delta u_i^{Lp}(\boldsymbol{x}) + \delta u_i^{Lq}(\boldsymbol{x})$ where local models Ω^{Lp} and Ω^{Lq} $(1 \le p, q \le M,\ p \ne q)$ overlap on the global model. δu_i^p $(1 \le p \le M)$ are set to be zero at the boundary $\partial\Omega^{Lp}$ of Ω^{Lp}.

Thus, the displacements and their variations are substituted in the statement of virtual work principle. After some algebraic manipulations, we arrive at:

$$\int_{\Omega^G} \frac{\partial \delta u_i^G}{\partial x_j} E_{ijk\ell} \frac{\partial u_k^G}{\partial x_\ell} \mathrm{d}\Omega^G + \sum_{p=1}^{M} \int_{\Omega^{Lp}} \frac{\partial \delta u_i^G}{\partial x_j} E_{ijk\ell} \frac{\partial u_k^{Lp}}{\partial x_\ell} \mathrm{d}\Omega^{Lp} = \int_{\Omega^G} \delta u_i^G b_i \mathrm{d}\Omega^G + \int_{\partial\Omega_t^G} \delta u_i \bar{t}_i \mathrm{d}\left(\partial\Omega_t^G\right) \tag{7}$$

$$\int_{\Omega^{Lp}} \frac{\partial \delta u_i^{Lp}}{\partial x_j} E_{ijk\ell} \frac{\partial u_k^G}{\partial x_\ell} \mathrm{d}\Omega^{Lp} + \int_{\Omega^{Lp}} \frac{\partial \delta u_i^{Lp}}{\partial x_j} E_{ijk\ell} \frac{\partial u_k^{Lp}}{\partial x_\ell} \mathrm{d}\Omega^{Lp} + \sum_{\substack{q=1 \\ q\ne p}}^{M} \int_{\Omega^{Lp-Lq}} \frac{\partial \delta u_i^{Lp}}{\partial x_j} E_{ijk\ell} \frac{\partial u_k^{Lq}}{\partial x_\ell} \mathrm{d}\Omega^{Lp-Lq} = \int_{\Omega^{Lp}} \delta u_i^{Lp} b_i \mathrm{d}\Omega^{Lp}$$

$$(p = 1,2,3,\cdots,M) \tag{8}$$

From the left hand sides of equations (7) and (8), various stiffness matrices are obtained. Thus, an equation can be written in a matrix form, as:

$$\begin{bmatrix} \boldsymbol{K}^G & \boldsymbol{K}^{G-L1} & \boldsymbol{K}^{G-L2} & \boldsymbol{K}^{G-L3} & \cdots & \boldsymbol{K}^{G-LM} \\ \boldsymbol{K}^{L1-G} & \boldsymbol{K}^{L1} & \boldsymbol{K}^{L1-L2} & \boldsymbol{K}^{L1-L3} & \cdots & \boldsymbol{K}^{L1-LM} \\ \boldsymbol{K}^{L2-G} & \boldsymbol{K}^{L2-L1} & \boldsymbol{K}^{L2} & \boldsymbol{K}^{L2-L3} & \cdots & \boldsymbol{K}^{L2-LM} \\ \boldsymbol{K}^{L3-G} & \boldsymbol{K}^{L3-L1} & \boldsymbol{K}^{L3-L2} & \boldsymbol{K}^{L3} & \cdots & \boldsymbol{K}^{L3-LM} \\ \vdots & \vdots & \vdots & \vdots & \ddots & \vdots \\ \boldsymbol{K}^{LM-G} & \boldsymbol{K}^{LM-L1} & \boldsymbol{K}^{LM-L2} & \boldsymbol{K}^{LM-L3} & \cdots & \boldsymbol{K}^{LM} \end{bmatrix} \begin{Bmatrix} \boldsymbol{u}^G \\ \boldsymbol{u}^{L1} \\ \boldsymbol{u}^{L2} \\ \boldsymbol{u}^{L3} \\ \vdots \\ \boldsymbol{u}^{LM} \end{Bmatrix} = \begin{Bmatrix} \boldsymbol{F}^G \\ \boldsymbol{F}^{L1} \\ \boldsymbol{F}^{L2} \\ \boldsymbol{F}^{L3} \\ \vdots \\ \boldsymbol{F}^{LM} \end{Bmatrix} \tag{9}$$

$\boldsymbol{K}^G$ is the ordinary stiffness matrix for the global finite element model which arises from the first term of equation (7) and $\boldsymbol{K}^{Lp}$ $(p = 1,2,3,\cdots,M)$ are those for the local finite element models arising from the second term of equation (8). $\boldsymbol{K}^{G-Lp}$ $(p = 1,2,3,\cdots,M)$ and $\boldsymbol{K}^{Lp-G}$ $(p = 1,2,3,\cdots,M)$ are the coupling stiffness matrices between the global and local finite element models, arising from the second term of equation (7) and the first term of equation (8), respectively. $\boldsymbol{K}^{Lp-Lq}$ $(p, q = 1,2,3,\cdots,M;\ p \ne q)$ are the coupling stiffness matrices between the local finite element models arising from the third term of equation (8). $\boldsymbol{F}^G$ and $\boldsymbol{F}^{Lp}$ $(p = 1,2,3,\cdots,M)$ are the nodal force vectors

of external and body forces. It is noted that the matrices have the properties of $\boldsymbol{K}^{Lp-G} = \left(\boldsymbol{K}^{G-Lp}\right)^T$ and $\boldsymbol{K}^{Lp-Lq} = \left(\boldsymbol{K}^{Lq-Lp}\right)^T$. Therefore, the coefficient matrix in the left hand side of equation (9) is symmetric.

Unknown nodal displacements are obtained by solving the linear simultaneous equations (9), and the displacement field in the composite is determined (see Okada, Liu, Ninomiya, Fukui and Kumazawa [5] for the full details of the solution procedures).

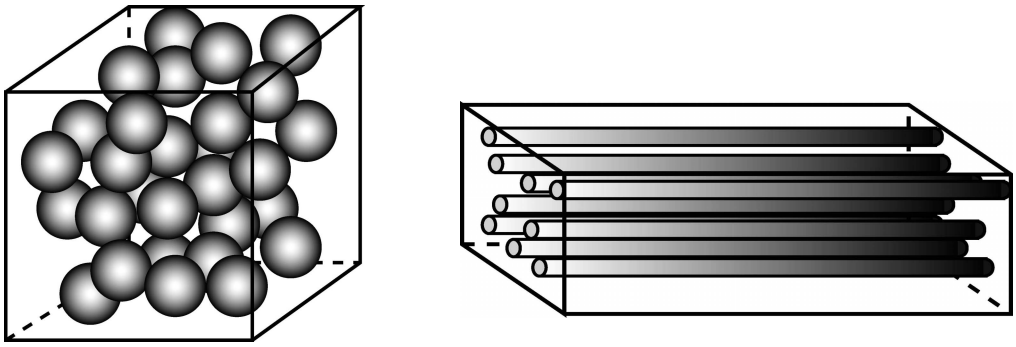

(a) Particulate composite (b) Fibrous composite

Figure 1 Schematic views of composite materials

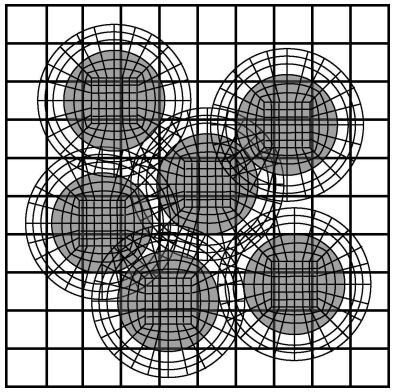

Figure 2 An s-FEM model for composite material in which each fiber/particle and its immediate vicinity are modeled by a local finite element mesh

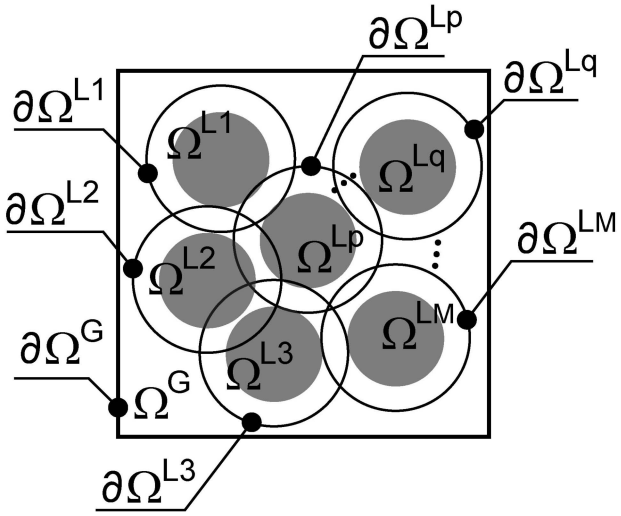

Figure 3 Local model regions ($\Omega^{Lp}\left(p=1,2,3,\cdots,M\right)$) which are superposed on the global model region Ω^{G}

1.2 Numerical Implementations of s-FEM (Evaluation of stiffness matrices)

A unique feature of the s-FEM is that elements in global and local finite element models overlap each other. There are many ways for elements to overlap, as shown in Figure 4. Elements may overlap each other in an arbitrary manner. This raises serious problems in the evaluation of stiffness matrices such that i) when a coupling stiffness matrix such as $\boldsymbol{K}^{Lp-Lq}$ is formed, elements in different finite element models may partially overlap each other (two-dimensional illustration is presented in Figure 5) and ii) more than one material models or material parameters that are specified by the overlapping elements may exist at a point. Some special care must be given to overcome these issues. In this section, how we can overcome these issues in s-FEM computer implementation is described.

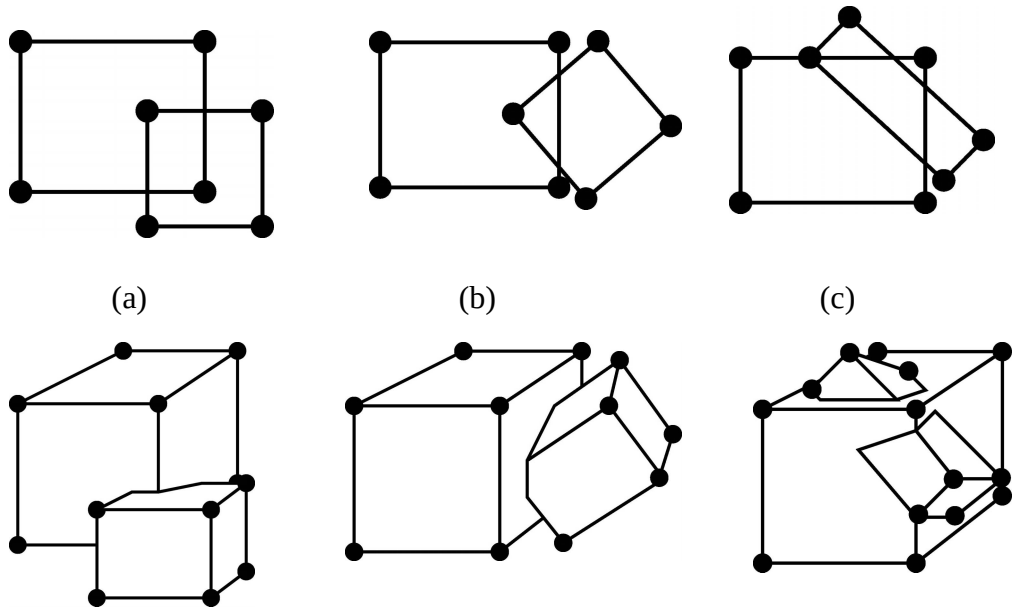

Figure 4 Many ways that two elements overlap each other; (a)~(c): Two-dimensional examples and (d)~(f): Three-dimensional examples

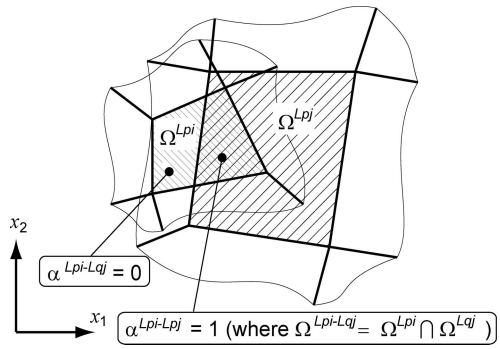

Figure 5 Overlapping region $\Omega^{LPi-Lqj}$ of the regions Ω^{Lpi} and Ω^{Lqj} of two elements (Lpi and Lpj)

1.2.1 Evaluation of element and coupling stiffness matrix

We consider a typical scenario. Figure 5 illustrates the finite elements *i* and *j* of the local mesh regions *p* and *q*. They are designated to be elements *Lpi* and *Lqj*, respectively. They overlap each other and, therefore, their coupling stiffness matrix is formed. The coupling stiffness matrix $\left[\boldsymbol{k}^{Lpi-Lqj}\right]$ can be written to be:

$$\left[\boldsymbol{k}^{Lpi-Lqj}\right] = \int_{\Omega^{Lpi-Lqj}} \left[\boldsymbol{B}^{Lpi}\right]^T [\boldsymbol{E}] \left[\boldsymbol{B}^{Lqj}\right] d\Omega^{Lpi-Lqj} \tag{10}$$

where $\left[\boldsymbol{B}^{Lpi}\right]$ and $\left[\boldsymbol{B}^{Lqj}\right]$ are the strain-displacement matrix for the elements, and $[\boldsymbol{E}]$ is the matrix representing the elastic constants $E_{ijk\ell}$ in equation (5). $\Omega^{Lpi-Lqj}$ is the volume of overlapping region. When the coupling stiffness matrix is formed, a numerical integration is performed for the overlapping volume $\Omega^{Lpi-Lqj}$.

However, the overlapped region $\Omega^{Lpi-Lqj}$ may have a complex geometry. It is almost impossible to explicitly define the geometry of the overlapping region and to apply an ordinary numerical integral scheme such as Gasuss quadrature. In this study, we perform the integral based on one of the overlapping elements. It can be shown to be:

$$\left[\boldsymbol{k}^{Lpi-Lqj}\right] = \int_{\Omega^{Lpi}} \alpha^{Lpi-Lqj}(\boldsymbol{x}) \left[\boldsymbol{B}^{Lpi}\right]^T [\boldsymbol{E}] \left[\boldsymbol{B}^{Lqj}\right] d\Omega^{Lpi} \tag{11}$$

$\alpha^{Lpi-Lqj}(\boldsymbol{x})$ is a scalar function whose value is “1” in $\Omega^{Lpi-Lqj}$ and “0” outside of $\Omega^{Lpi-Lqj}$, as indicated in Figure 5. Numerical integral is performed based on element *Lpi*. Therefore, the integrand of equation (11) has a sever discontinuity since the value of $\alpha^{Lpi-Lqj}(\boldsymbol{x})$ changes abruptly from “1” to “0” or “0” to “1”. Therefore, an ordinary Gauss quadrature is unable to evaluate the integral accurately. In order to circumvent this problem, we developed an element subdivision scheme.

The element subdivision technique is illustrated in Figure 6 for two- and three-dimensional problems. As shown in Figure 6 (a-i), two-dimensional elements *Lpi* and *Lqj* partially overlap each other, and the integration is performed based on *Lpi*. First, element *Lpi* is divided into 4 sub-cells. Then each subdivided-cell is checked if it intersects with the edges of element *Lqj*. If a subdivided-cell intersects with the edges of element *Lqj*, it is divided into 4 sub-cells again. This process is repeated until the smallest sub-cell becomes small enough (typically within 1% of the volume of element *Lpi*). The processes of creating sub-cells are shown in Figures 6 (a-ii)~(a-iv). Then, an ordinary Gauss quadrature rule is applied in each subdivided-cell. The same approach is adopted in three-dimensional problems, as shown in Figure 6 (b-i)-(b-iv). However, it should be noted that proposed methodology is not computationally efficient and takes much longer computational time than the ordinary Gauss quadrature, because many

integration points are used to carry out the numerical integral.

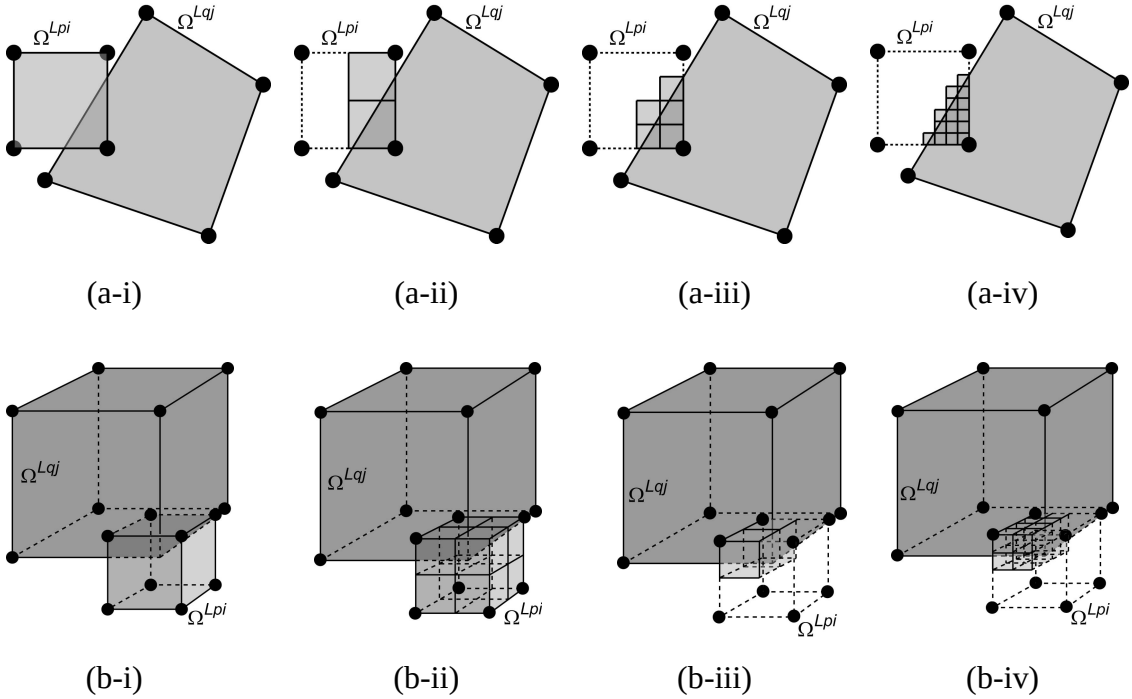

Figure 6 Element subdivision techniques for (a) two- and (b) three- dimensional problems

1.2.2 Material constants and strain histories

In an ordinary finite element method, the material constants are assigned to finite elements and the strain history information, such as damage paramters are stored at the integration points. In present s-FEM analysis, the global and local finite element models overlap each other and material data including initial strains and strain history parameters are assigned to global and local finite element models independently. This means that two or more sets of material parameters exist within an overlapping region. First, priority orders are assigned to material models in the input data. Deformation history data is stored at ordinary integration points in each element in global and local finite element model. When two or more finite elements overlap at a point, a material model having the highest propriety order is chosen first. If there were two or more overlapping elements having the same material model at a point, deformation history data of the smallest element is used to form the stiffness matrices.

For example, in Figure 7, a two-dimensional schematic illustration is given. There are two material models ***A*** and ***B*** that are assigned to the elements. At a point within the

overlapping region, material model ***A*** or ***B*** is chosen according to their assigned priority orders. Even when an ordinary element stiffness matrix is formed, abrupt changes in material constant may occur. The element subdivision scheme of section 1.2.1 is used for such cases.

Next, we discuss about treatments for the strain history parameters. When the element subdivision technique is adopted, many integration points just for numerical integration are generated. If one tries to store the strain history data at each one of them, a large amount of computer memory will be required. Thus, in present s-FEM program, each ordinary integration point carries the strain history information. For example, in the case of two-dimensional linear finite element, there are four ordinary integration points, as depicted in Figure 8. Figure 8 presents the positions of four integration points in ξ-η normalized coordinate system. Each of the integration points represents a quarter of area of the element as shown in Figure 8. When the element subdivision technique is used, the ξ-η normalized coordinate values of each generated integration point are evaluated and the program chooses an ordinary integration point whose strain history parameters are used. For three-dimensional case, the same strategy is adopted.

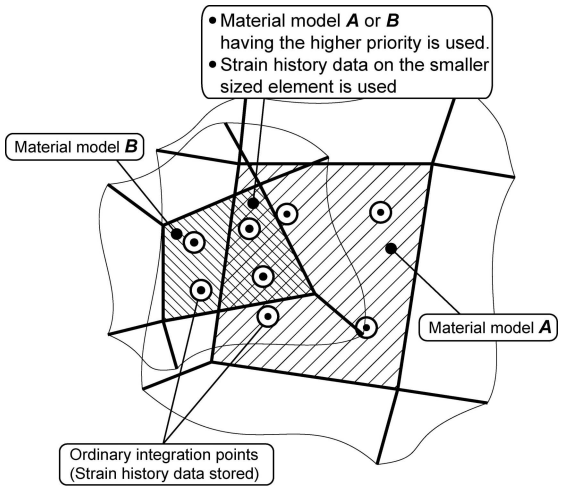

Figure 7 A region of multiply assignmed material models and the Gauss points in the overlapping elements

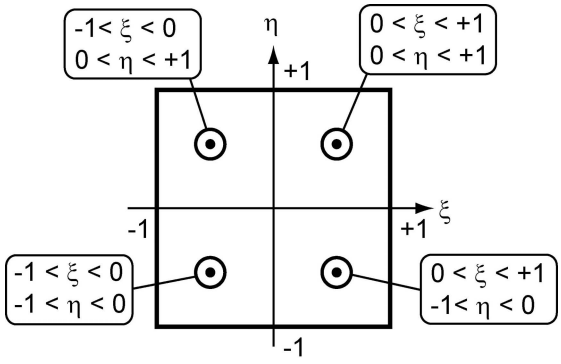

Figure 8 Gauss points in an element (two-dimensional quadrilateral element)

2. Damage constitutive model

In this research, we assume the nucleation and growth of microvoids in polymeric material and the dewetting between the particles and polymeric matrix material. Figure 9 shows the schematic view of damage modes. These material damages reduce the effective area of material section. Thus, the material stiffness is reduced gradually while progressive material damages take place.

Two kinds of damage constitutive laws were adopted. They are described in this chapter. The isotropic damage model following Simo and Ju [6, 7] was extended to separate dilatational/deviatoric damage model that can account for the dilatational and deviatoric components of damages separately. The separate dilatational/deviatoric damage model is especially powerful when the deformation of the material under an ambient pressure is analyzed.

The dilatational part of material damage is mainly due to the nucleation and growth of microvoids. It is considered that under negative hydrostatic stress, the nucleation and growth of microvoids do not occur. The dilatational damage model is assumed to be induced when the hydrostatic stress is positive.

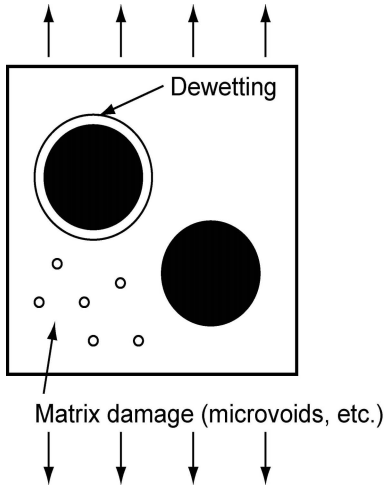

Figure 9 A schematic view of two kinds of damage modes; the growth of microvoids in matrix material and dewetting between the particles and matrix material

2.1 Isotropic damage constitutive model

First, we describe the isotropic damage theory by following Simo and Ju [6]. In Simo and Ju [6], the effective stress concept and the hypothesis of strain equivalence are described. When they are applied to the case of elastic damage, the elastic potential energy of damaged material, in terms of the strains ε_{ij} and the damage parameter d is written to be:

$$\psi(\varepsilon_{k\ell}, d) = (1-d)\psi^o(\varepsilon_{k\ell}) \tag{12}$$

where $\psi^o(\varepsilon_{k\ell})$ is the elastic-potential function for virgin material that is written to be:

$$\psi^o(\varepsilon_{k\ell}) = \frac{1}{2} C_{ijk\ell}\varepsilon_{ij}\varepsilon_{k\ell} \tag{13}$$

Just like equivalent stress concept in the theory of plasticity, a scalar parameter $\bar{\tau}$ that measures the magnitude of stress/deformation is introduced.

$$\bar{\tau} = \sqrt{2\psi^o(\varepsilon_{k\ell})} \tag{14}$$

Criteria for the damage evolution are written as follows. First, the effective stress needs to reach the critical value.

$$g(\bar{\tau}(\varepsilon_{k\ell}) - r(d)) = \bar{\tau}(\varepsilon_{k\ell}) - r(d) = 0 \tag{15}$$

where $r(d)$ is the function of the damage parameter d. The relationship between $r(d)$ and d needs to be determined based an experimental data. The material damage progresses when the damage parameter increases. Therefore, when the damage is ongoing, the time derivative of the damage parameter $\dot{d}$ must be positive.

$$\dot{d} > 0 \tag{16}$$

$\dot{d}$ is determined through the evolution law, as:

$$\dot{d} = \dot{r}H(\bar{\tau}, d) = \dot{\tau}(\varepsilon_{k\ell})H(\bar{\tau}, d) \tag{17}$$

The constant $H(\bar{\tau},d)$ characterizes the progress of damage with respect to the effective stress like term. Equations (15) and (16) must be satisfied when the progressive damage takes place. It is noted that the constant $H(\bar{\tau},d)$ is always positive. Therefore, the equivalent stress-like term must increase to satisfy equation (17), while the material damage is in progress.

Since the elastic potential energy is assumed in the form of equation (1), the stresses σ_{ij} are written in the following form.

$$\sigma_{ij} = (1-d)C_{ijk\ell}\varepsilon_{k\ell} \tag{18}$$

The rates of stresses can be expressed by differentiating both the sides of equation (12), as:

$$\dot{\sigma}_{ij} = (1-d)C_{ijk\ell}\dot{\varepsilon}_{k\ell} - \dot{d}C_{ijk\ell}\varepsilon_{k\ell} = (1-d)C_{ijk\ell}\dot{\varepsilon}_{k\ell} - \dot{d}\sigma^{o}_{ij} \tag{19}$$

where $\sigma^{o}_{ij}\left(=C_{ijk\ell}\varepsilon_{k\ell}\right)$ are the stresses when the virgin material is assumed for the same strains. From equation (17), the rate $\dot{d}$ of damage parameter d can be derived to be:

$$\dot{d} = \dot{\bar{\tau}}H(\bar{\tau},d) = H(\bar{\tau},d)\frac{\sigma^{o}_{k\ell}}{\bar{\tau}}\dot{\varepsilon}_{k\ell} = \frac{H(\bar{\tau},d)}{\bar{\tau}}\sigma^{o}_{k\ell}\dot{\varepsilon}_{k\ell} \tag{20}$$

$H(\bar{\tau},d)$ characterizes the rate of damage parameter d with respect to the rate of the effective stress-like parameter $\dot{\bar{\tau}}$.
Substituting equation (20) in equation (19), we arrive at:

$$\begin{aligned}\dot{\sigma}_{ij} &= (1-d)C_{ijk\ell}\dot{\varepsilon}_{k\ell} - \dot{d}\sigma^{o}_{ij} = (1-d)C_{ijk\ell}\dot{\varepsilon}_{k\ell} - \frac{H(\bar{\tau},d)}{\bar{\tau}}\sigma^{o}_{ij}\sigma^{o}_{k\ell}\dot{\varepsilon}_{k\ell} \\ &= D^{ID}_{ijk\ell}\dot{\varepsilon}_{k\ell}\end{aligned} \tag{21}$$

where

$$D^{ID}_{ijk\ell} = (1-d)C_{ijk\ell} - \frac{H(\bar{\tau},d)}{\bar{\tau}}\sigma^{o}_{ij}\sigma^{o}_{k\ell} \tag{22}$$

$D^{ID}_{ijk\ell}$ are the tangent moduli for the isotropic damage material and have the major and minor symmetries, i.e. $D^{ID}_{ijk\ell} = D^{ID}_{k\ell ij}$, $D^{ID}_{ijk\ell} = D^{ID}_{ij\ell k}$ and $D^{ID}_{ijk\ell} = D^{ID}_{jik\ell}$.

2.2 Separate Isotropic/deviatoric damage model

The damage evolution of some class of materials are more sensitive to hydrostatic pressure stress than shear stresses. A typical scenario is in a material containing microvoids. Microvoids grow under applied positive-hydrostatic pressure stress. But they do not grow under negative-hydrostatic pressure stress. The growths of the voids are assumed to be less sensitive to the shear (deviatoric) stresses than positive-hydrostatic stress.

One way to model such material is to separate the contributions of isotropic and deviatoric stresses to the damage growth. To do so with a very simple model, we separate the damage parameter d into the dilatational (volumetric) and deviatoric parts. Hence, the elastic potential energy function [equation (12)] is modified and is written to be:

$$\psi(\varepsilon_{k\ell}, d_V, d_D) = (1-d_V)\psi^{o}_{V}(\varepsilon_{kk}) + (1-d_D)\psi^{o}_{D}(\varepsilon'_{ij}) \tag{23}$$

where ε_{kk} and ε'_{ij} are the volumetric and deviatoric strains. The functions ψ^{o}_{V} and ψ^{o}_{D} are defined to be:

$$\psi^{o}_{V} = \frac{1}{2}K(\varepsilon_{kk})^2 \quad \text{and} \quad \psi^{o}_{V} = \mu\varepsilon'_{ij}\varepsilon'_{ij} \tag{24}$$

where K and μ are the bulk and shear moduli. It is noted here that under a constraint condition $d_V = d_D$, the separate dilatational/deviatoric damage model is the same as the isotropic damage model. We define two kinds of effective stress-like terms, as:

$$\bar{\tau}_V = \sqrt{2\psi_V^o(\varepsilon_{kk})} = \sqrt{K(\varepsilon_{kk})^2} \quad \text{and} \quad \bar{\tau}_D = \sqrt{2\psi_D^o(\varepsilon'_{ij})} = \sqrt{2\mu\varepsilon'_{ij}\varepsilon'_{ij}} \tag{25}$$

When the damages are in progress, the following conditions must be satisfied.

$$\bar{\tau}_V = r_v(d_v) \quad \text{and} \quad \sigma_{kk} > 0 \quad \text{for the dilatational damage} \tag{26}$$

$$\bar{\tau}_D = r_v(d_D) \quad \text{for the deviatoric damage} \tag{27}$$

The evolution equations for the damage parameters are written, as:

$$\dot{d}_V = \dot{\bar{\tau}}_V H_V(\bar{\tau}_V, d_V) = H_V(\bar{\tau}_V, d_V)\sqrt{K}\dot{\varepsilon}_{kk} = H_V(\bar{\tau}_V, d_V)\frac{K\varepsilon_{pp}}{\sqrt{K(\varepsilon_{qq})^2}}\dot{\varepsilon}_{kk} \tag{28}$$

$$\dot{d}_D = \dot{\bar{\tau}}_D H_D(\bar{\tau}_D, d_D) = H_D(\bar{\tau}_D, d_D)\frac{2\mu\varepsilon'_{k\ell}}{\sqrt{2\mu\varepsilon'_{pq}\varepsilon'_{pq}}}\varepsilon'_{k\ell} \tag{29}$$

The constants $H_V(\bar{\tau}_V, d_V)$ and $H_D(\bar{\tau}_D, d_D)$ govern the evolution laws for the damage parameters. The constants are the functions of the effective stress-like terms $\bar{\tau}_V$ and $\bar{\tau}_D$ and of the damage parameters d_V and d_D. From equation (23), we can write the stresses, as:

$$\sigma_{ij} = \frac{\partial\psi(\varepsilon_{k\ell}, d_V, d_D)}{\partial\varepsilon_{ij}} = (1-d_V)\delta_{ij}K\varepsilon_{kk} + 2(1-d_D)\mu\varepsilon'_{ij} \tag{30}$$

By differentiating both the sides of equation (30) and making use of equations (28) and (29), we can write the rate form constitutive equation, as:

$$\begin{aligned}\dot{\sigma}_{ij} &= (1-d_V)\delta_{ij}K\dot{\varepsilon}_{kk} + 2(1-d_D)\mu\dot{\varepsilon}'_{ij} - \dot{d}_V K\varepsilon_{kk} - 2\dot{d}_D\mu\varepsilon'_{ij} \\ &= (1-d_V)\delta_{ij}K\dot{\varepsilon}_{kk} + 2(1-d_D)\mu\dot{\varepsilon}'_{ij} - \delta_{ij}\frac{H_V(\bar{\tau}_V, d_V)}{\bar{\tau}_V}(K\varepsilon_{kk})^2\dot{\varepsilon}_{\ell\ell} - \frac{4H_D(\bar{\tau}_D, d_D)}{\bar{\tau}_D}\mu^2\varepsilon'_{ij}\varepsilon'_{k\ell}\dot{\varepsilon}'_{k\ell} \\ &= D_{ijk\ell}^{V-D}\dot{\varepsilon}_{k\ell}\end{aligned} \tag{31}$$

and,

$$D_{ijk\ell}^{V-D} = (1-d_V)K\delta_{ij}\delta_{k\ell} + (1-d_D)\mu\left(\delta_{ik}\delta_{j\ell} + \delta_{jk}\delta_{i\ell}\right) - \frac{H_V(\bar{\tau}_V, d_V)}{\bar{\tau}_V}(K\varepsilon_{kk})^2\delta_{ij}\delta_{k\ell} - \frac{4H_D(\bar{\tau}_D, d_D)}{\bar{\tau}_D}\mu^2\varepsilon'_{ij}\varepsilon'_{k\ell} \quad (32)$$

$D_{ijk\ell}^{V-D}$ are the tangent moduli that relate the rate of stresses to those of strains. It is noted that $D_{ijk\ell}^{V-D}$ have the major and minor symmetries, i.e. $D_{ijk\ell}^{V-D} = D_{k\ell ij}^{V-D}$, $D_{ijk\ell}^{V-D} = D_{ij\ell k}^{V-D}$ and $D_{ijk\ell}^{V-D} = D_{jik\ell}^{V-D}$.

3. Cohesive zone model and its implementation in the s-FEM computer program

The cohesive zone model was implemented in the s-FEM computer program. In present research, the cohesive zone model accounts for separation between the reinforcing particles and matrix material. In this section, the formulations of the cohesive zone model (Chandra [8], Foulk, Allen and Helms [9], etc.) along with the s-FEM are presented.

3.1 Cohesive zone model

Interface separation law is characterized by the cohesive zone model. The interface in a solid is depicted in Figure 10. We assume that such interface separation takes place while progressive dewetting between matrix and a particle occurs. A three-dimensional illustration is given in Figure 11. Here, we define two kinds of coordinate systems. One is the global coordinate system (x_1, x_2, x_3) which is fixed in the space and the other is local coordinate system $(\bar{x}_1, \bar{x}_2, \bar{x}_3)$ in which $\bar{x}_1$ and $\bar{x}_2$ are in the plane of the interface and $\bar{x}_3$ is perpendicular to the interface. We define upper and lower faces as depicted in Figure 11. The positive direction of the $\bar{x}_3$ coordinate and the normal direction $\boldsymbol{n}$ of the interface are defined as depicted in Figure 11. Their directions are defined from the lower to the upper surface. Relative displacements $\Delta\bar{u}_i^{CHZ}$ are defined as the difference of the displacements $\bar{u}_i^{CHZ+}$ and $\bar{u}_i^{CHZ-}$ of the upper and the lower faces, respectively. $\overline{(\bullet)}_i$ indicate that the components of the vector are written in the $(\bar{x}_1, \bar{x}_2, \bar{x}_3)$ local coordinate system.

$$\Delta\bar{u}_i^{CHZ} = \bar{u}_i^{CHZ+} - \bar{u}_i^{CHZ-} \tag{33}$$

By using the relative displacements $\Delta\bar{u}_i^{CHZ}$, we define a dimensionless parameter λ which characterizes the separation and the slips of the interface, as:

$$\lambda = \sqrt{\left(\frac{\Delta\bar{u}_1^{CHZ}}{\delta t}\right)^2 + \left(\frac{\Delta\bar{u}_2^{CHZ}}{\delta t}\right)^2 + \left(\frac{\Delta\bar{u}_3^{CHZ}}{\delta n}\right)^2} \tag{34}$$

where δt and δn are the length parameters that characterizes the distance of partial

separation before the final one. Then, an energy density function is defined in terms of λ.

$$W^{CHZ} = W^{CHZ}(\lambda) \tag{35}$$

$W^{CHZ} = W^{CHZ}(\lambda)$ is the energy potential and has properties of:

$$\begin{aligned} &W^{CHZ}(\lambda = 0) = 0 \\ &W^{CHZ}(\lambda \to \infty) = W^{CHZ}\big|_{\text{Separation}} \end{aligned} \tag{36}$$

$W^{CHZ}\big|_{\text{Separation}}$ is the energy required to open unit area in cohesive zone.

Since $W^{CHZ} = W^{CHZ}(\lambda)$ represents the energy, we can express:

$$\dot{W}^{CHZ}(\lambda) = \frac{\partial W^{CHZ}}{\partial\left(\Delta\bar{u}_\alpha^{CHZ}\right)}\Delta\dot{\bar{u}}_\alpha^{CHZ} + \frac{\partial W^{CHZ}}{\partial\left(\Delta\bar{u}_3^{CHZ}\right)}\Delta\dot{\bar{u}}_3^{CHZ} \qquad (\alpha = 1,2) \tag{37}$$

Therefore, cohesive tractions $\bar{T}_i$ are written to be:

$$\bar{T}_\alpha = \frac{\partial W^{CHZ}}{\partial\left(\Delta\bar{u}_\alpha^{CHZ}\right)} \qquad (\alpha = 1,2), \qquad \bar{T}_3 = \frac{\partial W^{CHZ}}{\partial\left(\Delta\bar{u}_3^{CHZ}\right)} \tag{38}$$

Thus, we can express $\bar{T}_i$, as:

$$\bar{T}_\alpha = \frac{\partial W^{CHZ}}{\partial\left(\Delta\bar{u}_\alpha^{CHZ}\right)} = \frac{dW^{CHZ}}{d\lambda}\frac{\partial\lambda}{\partial\left(\Delta\bar{u}_\alpha^{CHZ}\right)} = \frac{dW^{CHZ}}{d\lambda}\frac{\Delta\bar{u}_\alpha^{CHZ}}{\delta_t^2}\frac{1}{\lambda} = \frac{dW^{CHZ}}{d\lambda}\frac{\Delta\bar{u}_\alpha^{CHZ}}{\lambda\delta_t^2} \tag{39}$$

$$\bar{T}_3 = \frac{\partial W^{CHZ}}{\partial\left(\Delta\bar{u}_3^{CHZ}\right)} = \frac{dW^{CHZ}}{d\lambda}\frac{\partial\lambda}{\partial\left(\Delta\bar{u}_3^{CHZ}\right)} = \frac{dW^{CHZ}}{d\lambda}\frac{\Delta\bar{u}_3^{CHZ}}{\delta_n^2}\frac{1}{\lambda} = \frac{dW^{CHZ}}{d\lambda}\frac{\Delta\bar{u}_3^{CHZ}}{\lambda\delta_n^2} \tag{40}$$

It is assumed here that W^{CHZ} has the following form:

$$W^{CHZ}(\lambda) = \delta_n\sigma_n^{MAX} f(\lambda) \tag{41}$$

Here, σ_n^{MAX} is the maximum normal stress and the maximum value of $f(\lambda)$ is one. $f(\lambda)$ is the dimensionless function of λ. The function $f(\lambda)$ takes its values $f(\lambda = 0) = 0$ and $f(\lambda \to \infty) = 0$. By using equation (41), the tractions can be written, as:

$$\begin{aligned}\overline{T}_\alpha &= \frac{\partial W^{CHZ}}{\partial\left(\Delta\bar{u}_\alpha^{CHZ}\right)} = \frac{dW^{CHZ}}{d\lambda}\frac{\partial\lambda}{\partial\left(\Delta\bar{u}_\alpha^{CHZ}\right)} = \frac{dW^{CHZ}}{d\lambda}\frac{\Delta\bar{u}_\alpha^{CHZ}}{\delta_t^2}\frac{1}{\lambda} = \delta_n\sigma_n^{MAX}\frac{df(\lambda)}{d\lambda}\frac{\Delta\bar{u}_\alpha^{CHZ}}{\lambda\delta_t^2} \\ &= \left(\frac{\delta_n}{\delta_t}\right)\sigma_n^{MAX}\frac{\Delta\bar{u}_\alpha^{CHZ}}{\delta_t}\frac{1}{\lambda}\frac{df(\lambda)}{d\lambda}\end{aligned} \tag{42}$$

$$\begin{aligned}\overline{T}_3 &= \frac{\partial W^{CHZ}}{\partial\left(\Delta\bar{u}_3^{CHZ}\right)} = \frac{dW^{CHZ}}{d\lambda}\frac{\partial\lambda}{\partial\left(\Delta\bar{u}_3^{CHZ}\right)} = \frac{dW^{CHZ}}{d\lambda}\frac{\Delta\bar{u}_3^{CHZ}}{\delta_n^2}\frac{1}{\lambda} = \delta_n\sigma_n^{MAX}\frac{df(\lambda)}{d\lambda}\frac{\Delta\bar{u}_3^{CHZ}}{\lambda\delta_n^2} \\ &= \sigma_n^{MAX}\frac{\Delta\bar{u}_3^{CHZ}}{\delta_n}\frac{1}{\lambda}\frac{df(\lambda)}{d\lambda}\end{aligned} \tag{43}$$

In many literatures such as [8] and [9], equations (42) and (43) are interpreted to be:

$$\overline{T}_\alpha = \alpha\sigma_n^{MAX}F(\lambda)\frac{\Delta\bar{u}_\alpha^{CHZ}}{\delta_t} \tag{44}$$

$$\overline{T}_3 = \sigma_n^{MAX}F(\lambda)\frac{\Delta\bar{u}_3^{CHZ}}{\delta_n} \tag{45}$$

where,

$$\alpha = \frac{\delta_n}{\delta_t} \tag{46}$$

Or we can write:

$$\overline{T}_\alpha = \frac{\delta_n}{\delta_t}\sigma_n^{MAX}F(\lambda)\frac{\Delta\bar{u}_\alpha^{CHZ}}{\delta_t} \tag{47}$$

$$\overline{T}_3 = \sigma_n^{MAX}F(\lambda)\frac{\Delta\bar{u}_3^{CHZ}}{\delta_n} \tag{48}$$

In order to obtain rate form tangent moduli, we further differentiate equations (47) and (48) with respect to time.

$$\begin{aligned}\dot{\overline{T}}_\alpha = \frac{1}{\delta_t}\sigma_n^{MAX}\Bigg\{&\frac{\delta_n}{\delta_t}F(\lambda)\Delta\dot{\bar{u}}_\alpha^{CHZ} \\ &+\frac{1}{\lambda}\frac{\mathrm{d}F(\lambda)}{\mathrm{d}\lambda}\left(\frac{\delta_n}{\delta_t}\frac{\Delta\bar{u}_\alpha^{CHZ}\Delta\bar{u}_1^{CHZ}}{\delta_t^2}\Delta\dot{\bar{u}}_1^{CHZ} + \frac{\delta_n}{\delta_t}\frac{\Delta\bar{u}_\alpha^{CHZ}\Delta\bar{u}_2^{CHZ}}{\delta_t^2}\Delta\dot{\bar{u}}_2^{CHZ} + \frac{\Delta\bar{u}_\alpha^{CHZ}\Delta\bar{u}_3^{CHZ}}{\delta_t\,\delta_n}\Delta\dot{\bar{u}}_3^{CHZ}\right)\Bigg\}\end{aligned} \tag{49}$$

Likewise,

$$\dot{T}_3 = \frac{1}{\delta_n}\sigma_n^{MAX}\left\{F(\lambda)\Delta\dot{\bar{u}}_3^{CHZ} + \frac{1}{\lambda}\frac{\mathrm{d}F(\lambda)}{\mathrm{d}\lambda}\left(\frac{\Delta\bar{u}_3^{CHZ}\Delta\bar{u}_1^{CHZ}}{\delta_t^2}\Delta\dot{\bar{u}}_1^{CHZ} + \frac{\Delta\bar{u}_3^{CHZ}\Delta\bar{u}_2^{CHZ}}{\delta_t^2}\Delta\dot{\bar{u}}_2^{CHZ} + \frac{\Delta\bar{u}_3^{CHZ}\Delta\bar{u}_3^{CHZ}}{\delta_n^2}\Delta\dot{\bar{u}}_3^{CHZ}\right)\right\} \tag{50}$$

In a matrix form, we can write:

$$\begin{Bmatrix}\dot{\bar{T}}_1\\ \dot{\bar{T}}_2\\ \dot{\bar{T}}_3\end{Bmatrix} = \sigma_n^{MAX}\left\{F(\lambda)\begin{bmatrix}\frac{1}{\delta_t} & 0 & 0\\ 0 & \frac{1}{\delta_t} & 0\\ 0 & 0 & \frac{1}{\delta_n}\end{bmatrix} + \frac{1}{\lambda}\frac{\mathrm{d}F(\lambda)}{\mathrm{d}\lambda}\begin{bmatrix}\frac{1}{\delta_t}\frac{\delta_n}{\delta_t}\frac{\Delta\bar{u}_1^{CHZ}\Delta\bar{u}_1^{CHZ}}{\delta_t^2} & \frac{1}{\delta_t}\frac{\delta_n}{\delta_t}\frac{\Delta\bar{u}_1^{CHZ}\Delta\bar{u}_2^{CHZ}}{\delta_t^2} & \frac{1}{\delta_t}\frac{\Delta\bar{u}_1^{CHZ}\Delta\bar{u}_3^{CHZ}}{\delta_t\,\delta_n}\\ \frac{1}{\delta_t}\frac{\delta_n}{\delta_t}\frac{\Delta\bar{u}_2^{CHZ}\Delta\bar{u}_1^{CHZ}}{\delta_t^2} & \frac{1}{\delta_t}\frac{\delta_n}{\delta_t}\frac{\Delta\bar{u}_2^{CHZ}\Delta\bar{u}_2^{CHZ}}{\delta_t^2} & \frac{1}{\delta_t}\frac{\Delta\bar{u}_2^{CHZ}\Delta\bar{u}_3^{CHZ}}{\delta_t\,\delta_n}\\ \frac{1}{\delta_t}\frac{\Delta\bar{u}_3^{CHZ}\Delta\bar{u}_1^{CHZ}}{\delta_n\delta_t} & \frac{1}{\delta_t}\frac{\Delta\bar{u}_3^{CHZ}\Delta\bar{u}_2^{CHZ}}{\delta_n\delta_t} & \frac{1}{\delta_n}\frac{\Delta\bar{u}_3^{CHZ}\Delta\bar{u}_3^{CHZ}}{\delta_n^2}\end{bmatrix}\right\}\begin{Bmatrix}\Delta\dot{\bar{u}}_1^{CHZ}\\ \Delta\dot{\bar{u}}_2^{CHZ}\\ \Delta\dot{\bar{u}}_3^{CHZ}\end{Bmatrix} \tag{51}$$

Therefore, the tangent matrix in the rate formulation is symmetric.

Function $F(\lambda)$ have some choices as described in Chandra [8]. In present analyses, following Foulk, Allen and Helms [9], we let $F(\lambda)$ be:

$$F(\lambda) = \frac{27}{4}\left(1 - 2\lambda + \lambda^2\right) \tag{52}$$

and therefore, $\dfrac{\mathrm{d}F(\lambda)}{\mathrm{d}\lambda} = \dfrac{27}{4}(-2 + 2\lambda) = \dfrac{27}{2}(\lambda - 1)$

In order to show the significance of this choice of function $F(\lambda)$, we consider the energy per unit area of the interface due to an opening mode. For the absence of $\Delta\bar{u}_1^{CHZ}$ and $\Delta\bar{u}_2^{CHZ}$ components, we can compute the energy Q, as:

$$Q = \int_0^{\delta_3} T_3 \mathrm{d}\left(\Delta\bar{u}_3^{CHZ}\right) = \int_0^1 \bar{T}_3\delta_n \mathrm{d}\lambda = \int_0^1 \sigma_n^{MAX}\delta_n\lambda\frac{27}{4}\left(1 - 2\lambda + \lambda^2\right)\mathrm{d}\lambda = \frac{27}{48}\sigma_n^{MAX}\delta_n \tag{53}$$

where

$$\bar{T}_3 = \sigma_n^{MAX} F(\lambda) \frac{\Delta \bar{u}_3^{CHZ}}{\delta_n} = \sigma_n^{MAX} F(\lambda)\lambda = \sigma_n^{MAX} \frac{27}{4}\left(1 - 2\lambda + \lambda^2\right)\lambda \tag{54}$$

and

$$\mathrm{d}\left(\Delta \bar{u}_3^{CHZ}\right) = \delta_n \mathrm{d}\lambda \tag{55}$$

From the expression of (54), the maximum value of T_3 is σ_n^{MAX} for $\lambda = \frac{1}{3}$.

From equations (53), (54) and (55), one can state:

- σ_n^{MAX} and δ_n determines the characteristics in normal separation (energy and initial stiffness of the interface).
- $\frac{\sigma_n^{MAX}}{\delta_n}$ characterizes the initial stiffness of the interface.

In addition, by examining equation (50), one can find that $\frac{\delta_n}{\delta_t}$ characterizes the stiffness ratio between the normal and the tangential separations of the interface.

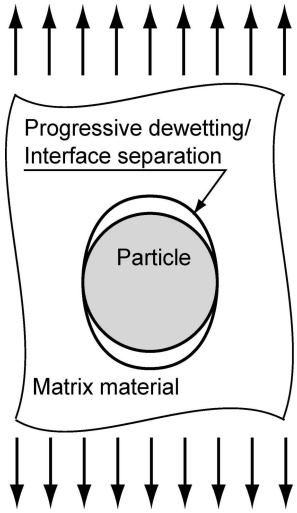

Figure 10 Progressive dewetting/interface separation between a particle and matrix material

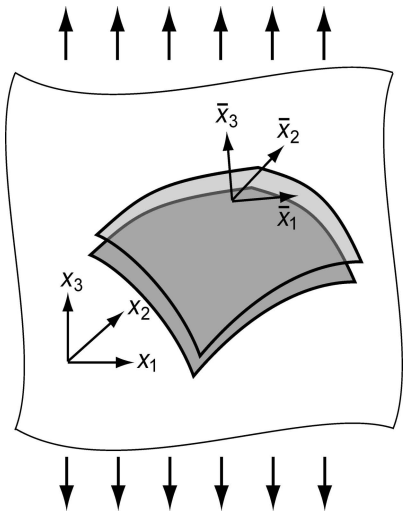

Figure 11 The cohesive zone and associated coordinate systems ((x_1, x_2, x_3) global and $(\bar{x}_1, \bar{x}_2, \bar{x}_3)$ local coordinate systems)

3.2 Cohesive zone with an arbitrary orientation

In the previous section, the cohesive zone model was described in the $(\bar{x}_1, \bar{x}_2, \bar{x}_3)$ local coordinate system. In this section, detailed discussions on how the coordinate translations from the local to the global coordinate system are carried out are given.

We assume a rate form formulation and the rates of stresses on the interface are written in terms of the rates of relative displacements.

$$\dot{\bar{T}}_i = \bar{k}_{ij} \Delta \dot{\bar{u}}_j^{CHZ} \tag{56}$$

where the components of $\bar{k}_{ij}$ are found from equation (51), as:

$$\begin{bmatrix} \bar{k}_{11} & \bar{k}_{12} & \bar{k}_{13} \\ \bar{k}_{21} & \bar{k}_{22} & \bar{k}_{23} \\ \bar{k}_{31} & \bar{k}_{32} & \bar{k}_{33} \end{bmatrix} = \sigma_n^{MAX} \left\{ F(\lambda) \begin{bmatrix} \frac{1}{\delta_t} & 0 & 0 \\ 0 & \frac{1}{\delta_t} & 0 \\ 0 & 0 & \frac{1}{\delta_n} \end{bmatrix} \right.$$

$$\left. + \frac{1}{\lambda} \frac{\mathrm{d}F(\lambda)}{\mathrm{d}\lambda} \begin{bmatrix} \frac{1}{\delta_t}\frac{\delta_n}{\delta_t}\frac{\Delta\bar{u}_1^{CHZ}\Delta\bar{u}_1^{CHZ}}{\delta_t^2} & \frac{1}{\delta_t}\frac{\delta_n}{\delta_t}\frac{\Delta\bar{u}_1^{CHZ}\Delta\bar{u}_2^{CHZ}}{\delta_t^2} & \frac{1}{\delta_t}\frac{\Delta\bar{u}_1^{CHZ}\Delta\bar{u}_3^{CHZ}}{\delta_t\,\delta_n} \\ \frac{1}{\delta_t}\frac{\delta_n}{\delta_t}\frac{\Delta\bar{u}_2^{CHZ}\Delta\bar{u}_1^{CHZ}}{\delta_t^2} & \frac{1}{\delta_t}\frac{\delta_n}{\delta_t}\frac{\Delta\bar{u}_2^{CHZ}\Delta\bar{u}_2^{CHZ}}{\delta_t^2} & \frac{1}{\delta_t}\frac{\Delta\bar{u}_2^{CHZ}\Delta\bar{u}_3^{CHZ}}{\delta_t\,\delta_n} \\ \frac{1}{\delta_t}\frac{\Delta\bar{u}_3^{CHZ}\Delta\bar{u}_1^{CHZ}}{\delta_n\,\delta_t} & \frac{1}{\delta_t}\frac{\Delta\bar{u}_3^{CHZ}\Delta\bar{u}_2^{CHZ}}{\delta_n\,\delta_t} & \frac{1}{\delta_n}\frac{\Delta\bar{u}_3^{CHZ}\Delta\bar{u}_3^{CHZ}}{\delta_n^2} \end{bmatrix} \right\} \tag{57}$$

When the interface is oriented in an arbitrary direction, matrix $\bar{k}_{ij}$ in the $(\bar{x}_1, \bar{x}_2, \bar{x}_3)$ local coordinate system must be transformed to the c global coordinate system. The directions of $\bar{x}_1$ and $\bar{x}_2$ coordinate axes are in the plane of the interface. $\bar{x}_3$ is perpendicular to the interface.

An inter-element face constitutes a cohesive zone element. The local normalized coordinates $(\xi - \eta)$, the local coordinates $(\bar{x}_1, \bar{x}_2, \bar{x}_3)$ and the global coordinates (x_1, x_2, x_3) are set as shown in Figure 12. Unit basis vectors with respect to the $(\bar{x}_1, \bar{x}_2, \bar{x}_3)$ and (x_1, x_2, x_3) coordinate systems are designated to be $(\bar{\boldsymbol{e}}_1, \bar{\boldsymbol{e}}_2, \bar{\boldsymbol{e}}_3)$ and $(\boldsymbol{e}_1, \boldsymbol{e}_2, \boldsymbol{e}_3)$, respectively.

First, we let the directions of ξ and $\bar{x}_1$ coordinate axes be the same, as shown in Figure 12. Thus, the basis vector $\bar{\boldsymbol{e}}_1$ is shown to be:

$$\bar{\boldsymbol{e}}_1 = \left(\frac{\partial x_i}{\partial \xi} \boldsymbol{e}_i \right) \Big/ \left| \frac{\partial x_i}{\partial \xi} \boldsymbol{e}_i \right| \tag{58}$$

Then, we define another unit vector $\hat{\boldsymbol{e}}_2$, and $\bar{\boldsymbol{e}}_2$ and $\bar{\boldsymbol{e}}_3$ are calculated to be:

$$\hat{\boldsymbol{e}}_2 = \left(\frac{\partial x_i}{\partial \eta} \boldsymbol{e}_i \right) \Big/ \left| \frac{\partial x_i}{\partial \eta} \boldsymbol{e}_i \right|, \quad \text{and} \quad \bar{\boldsymbol{e}}_3 = (\bar{\boldsymbol{e}}_1 \times \hat{\boldsymbol{e}}_2) / |\bar{\boldsymbol{e}}_1 \times \hat{\boldsymbol{e}}_2|, \quad \bar{\boldsymbol{e}}_2 = \bar{\boldsymbol{e}}_3 \times \bar{\boldsymbol{e}}_1 \tag{59}$$

The components $\bar{k}_{ij}$ of tangential stiffness of the cohesive zone are transformed to the global coordinate system, as:

$$k_{ij} = \boldsymbol{e}_i \cdot \left(\bar{k}_{k\ell}\bar{\boldsymbol{e}}_k\bar{\boldsymbol{e}}_\ell\right)\cdot \boldsymbol{e}_j = \bar{k}_{k\ell}\left(\bar{\boldsymbol{e}}_k \cdot \boldsymbol{e}_i\right)\left(\bar{\boldsymbol{e}}_\ell \cdot \boldsymbol{e}_j\right) \tag{60}$$

k_{ij} show the stiffness of the cohesive zone in the (x_1, x_2, x_3) global coordinate system.

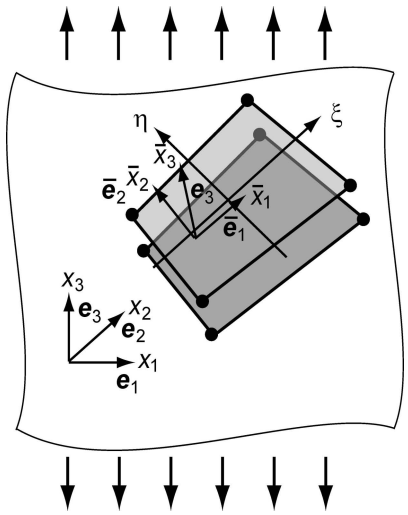

Figure 12 The $(\bar{x}_1, \bar{x}_2, \bar{x}_3)$ local coordinate system and its unit basis vectors $(\bar{\boldsymbol{e}}_1, \bar{\boldsymbol{e}}_2, \bar{\boldsymbol{e}}_3)$, and $(\xi - \eta)$ normalized coordinates

3.3 S-FEM formulation with the cohesive zone model

3.3.1 Formulations

The cohesive zone model is implemented in the s-FEM computer program. It is assumed that the cohesive zones are only implemented in the local finite element models. The global finite element model is not responsible for the cohesive zone model. In the s-FEM formulation, we start with the principle of virtual work, as stated below.

$$\int_{\Omega^G} \frac{\partial \delta u_i}{\partial x_j} E_{ijk\ell} \frac{\partial u_k}{\partial x_\ell} \mathrm{d}\Omega^G = \int_{\Omega^G} \delta u_i b_i \mathrm{d}\Omega^G + \int_{\partial\Omega_t^G} \delta u_i \bar{t}_i d\left(\partial\Omega_t^G\right) + \int_{S^{CHZ+}} \dot{t}_i^{CHZ+} \delta\dot{u}_i^{CHZ+} \mathrm{d}\left(S^{CHZ+}\right) + \int_{S^{CHZ-}} \dot{t}_i^{CHZ-} \delta\dot{u}_i^{CHZ-} \mathrm{d}\left(S^{CHZ-}\right) \tag{61}$$

where S^{CHZ+} and S^{CHZ-} are both the faces of the cohesive zone. $\dot{t}_i^{CHZ+}$ and $\dot{t}_i^{CHZ-}$ are the rate of tractions on S^{CHZ+} and S^{CHZ-}, respectively, that are induced by the opening of the cohesive zone. $\delta\dot{u}_i^{CHZ+}$ and $\delta\dot{u}_i^{CHZ-}$ are the variations of the displacement rates on S^{CHZ+} and S^{CHZ-}. They are in the state of equilibrium and therefore we can write:

$$\dot{t}_i^{CHZ+} = -\dot{t}_i^{CHZ-} \tag{62}$$

Therefore, we have:

$$\int_{S^{CHZ+}} \dot{t}_i^{CHZ+} \delta\dot{u}_i^{CHZ+} \mathrm{d}\left(S^{CHZ+}\right) + \int_{S^{CHZ-}} \dot{t}_i^{CHZ-} \delta\dot{u}_i^{CHZ-} \mathrm{d}\left(S^{CHZ-}\right) = \int_{S^{CHZ+}} \dot{t}_i^{CHZ+} \left(\delta\dot{u}_i^{CHZ+} - \delta\dot{u}_i^{CHZ-}\right) \mathrm{d}\left(S^{CHZ+}\right) \tag{63}$$

The traction rates $\dot{t}_i^{CHZ+}$ are written in terms of the rates of relative displacements $\Delta\dot{\bar{u}}_i^{CHZ}$ on the cohesive zone, as shown in equation (56). The relative displacements are written in terms of jumps in the displacements across the cohesive zone. Thus, $\dot{t}_i^{CHZ+}$ are written to be:

$$\dot{t}_i^{CHZ+} = -k_{ij}\left(\dot{u}_j^{CHZ+} - \dot{u}_j^{CHZ-}\right) \tag{64}$$

Where $\dot{u}_j^{CHZ+}$ and $\dot{u}_j^{CHZ-}$ are the velocities at both the faces of the cohesive zone. k_{ij} are the tangent stiffness of the cohesive zone, as described in previous section. The right hand side of equation (64) has a negative sign because the positive direction of the surface is opposite from that in previous section. By substituting equation (64) and by using the superposition of displacements based on the global and local finite element models, we can write:

$$\int_{\Omega^G} \frac{\partial \delta u_i^G}{\partial x_j} E_{ijk\ell} \frac{\partial u_k^G}{\partial x_\ell} \mathrm{d}\Omega^G + \sum_{p=1}^{M} \int_{\Omega^{Lp}} \frac{\partial \delta u_i^G}{\partial x_j} E_{ijk\ell} \frac{\partial u_k^{Lp}}{\partial x_\ell} \mathrm{d}\Omega^{Lp} = \int_{\Omega^G} \delta u_i^G b_i \mathrm{d}\Omega^G + \int_{\partial\Omega_t^G} \delta u_i \bar{t}_i \mathrm{d}\left(\partial\Omega_t^G\right) \tag{65}$$

$$\int_{\Omega^{Lp}} \frac{\partial \delta u_i^{Lp}}{\partial x_j} E_{ijk\ell} \frac{\partial u_k^{G}}{\partial x_\ell} \mathrm{d}\Omega^{Lp} + \int_{\Omega^{Lp}} \frac{\partial \delta u_i^{Lp}}{\partial x_j} E_{ijk\ell} \frac{\partial u_k^{Lp}}{\partial x_\ell} \mathrm{d}\Omega^{Lp} + \sum_{\substack{q=1 \\ q\neq p}}^{M} \int_{\Omega^{Lp-Lq}} \frac{\partial \delta u_i^{Lp}}{\partial x_j} E_{ijk\ell} \frac{\partial u_k^{Lq}}{\partial x_\ell} \mathrm{d}\Omega^{Lp-Lq}$$
$$+ \int_{S^{CHZ+}} \left(\delta u_i^{CHZ+(Lp)} - \delta u_i^{CHZ-(Lp)}\right) k_{ij} \left(u_j^{CHZ+(Lp)} - \delta u_j^{CHZ-(Lp)}\right) \mathrm{d}\left(S^{CHZ+(Lp)}\right) = \int_{\Omega^{Lp}} \delta u_i^{Lp} b_i \mathrm{d}\Omega^{Lp} \tag{66}$$
$$\left(p = 1,2,3,\cdots,M\right)$$

Here, we assume that there are *M* local models that are superposed on the global model. The local models may overlap each other and their coupling terms appear in equation (66). It is noted that though the cohesive zones of different local model regions may intersect each other, their coupling terms do not appear in equation (66). That is because two cohesive zones make a line of intersection when they intersect and the line has a zero area.

3.3.2 Cohesive zone element

When the cohesive zone is implemented in the s-FEM computer program, we introduce a concept of cohesive zone element. The cohesive zone element behaves like an interface element. Figure 13 shows the cohesive zone element. For an illustrative purpose, the cohesive zone element in Figure 13 a small thickness. In actual model, the thickness is zero.

The terms that are related with the cohesive zone element in equation (66) as expanded further, as:

$$\begin{aligned}
&\int_{S^{CHZ+}} \left(\delta \dot{u}_i^{CHZ+(Lp)} - \delta \dot{u}_i^{CHZ-(Lp)}\right) k_{ij} \left(\dot{u}_j^{CHZ+(Lp)} - \delta \dot{u}_j^{CHZ-(Lp)}\right) \mathrm{d}\left(S^{CHZ+(Lp)}\right) \\
&= \int_{S^{CHZ+}} \delta \dot{u}_i^{CHZ+(Lp)} k_{ij} \dot{u}_j^{CHZ+(Lp)} \mathrm{d}\left(S^{CHZ+(Lp)}\right) - \int_{S^{CHZ+}} \delta \dot{u}_i^{CHZ+(Lp)} k_{ij} \dot{u}_j^{CHZ-(Lp)} \mathrm{d}\left(S^{CHZ+(Lp)}\right) \\
&- \int_{S^{CHZ+}} \delta \dot{u}_i^{CHZ-(Lp)} k_{ij} \dot{u}_j^{CHZ+(Lp)} \mathrm{d}\left(S^{CHZ+(Lp)}\right) + \int_{S^{CHZ+}} \delta \dot{u}_i^{CHZ-(Lp)} k_{ij} \dot{u}_j^{CHZ-(Lp)} \mathrm{d}\left(S^{CHZ+(Lp)}\right)
\end{aligned} \tag{67}$$

Discretization procedures for the first term in the right hand side of equation (67) are described, as an example. Element stiffness matrix for a cohesive zone element $S^{CHZ+(Lp)}$ is derived as follows. The displacements within $S^{CHZ+(Lp)}$ are expressed by using the shape functions $N^I \left(I = 1,2,3,4\right)$ where the CHZ element is assumed to be linear quadrilateral element.

$$\dot{u}_i = \left[\boldsymbol{N}\right] \left\{\boldsymbol{u}^{(1\sim4)}\right\} \tag{68}$$

The detail of equation (68) can be written to be:

$$\begin{Bmatrix} \dot{u}_1 \\ \dot{u}_2 \\ \dot{u}_3 \end{Bmatrix} = \begin{bmatrix} N^1 & 0 & 0 & N^2 & 0 & 0 & N^3 & 0 & 0 & N^4 & 0 & 0 \\ 0 & N^1 & 0 & 0 & N^2 & 0 & 0 & N^3 & 0 & 0 & N^4 & 0 \\ 0 & 0 & N^1 & 0 & 0 & N^2 & 0 & 0 & N^3 & 0 & 0 & N^4 \end{bmatrix} \begin{Bmatrix} \dot{u}_1^1 \\ \dot{u}_2^1 \\ \dot{u}_3^1 \\ \dot{u}_1^2 \\ \dot{u}_2^2 \\ \dot{u}_3^2 \\ \dot{u}_1^3 \\ \dot{u}_2^3 \\ \dot{u}_3^3 \\ \dot{u}_1^4 \\ \dot{u}_2^4 \\ \dot{u}_3^4 \end{Bmatrix} \tag{69}$$

The superscripts in equation (69) designate the nodal numbers (1, 2, 3 or 4).
The variations of the velocities can also be written in the same manner. The stiffness of the CHZ can be written in a matrix from, as:

$$[\boldsymbol{k}] = \begin{bmatrix} k_{11} & k_{12} & k_{13} \\ k_{21} & k_{22} & k_{23} \\ k_{31} & k_{32} & k_{33} \end{bmatrix} \tag{70}$$

Thus, we have:

$$\begin{aligned} \int_{S^{CHZ+}} \delta\dot{u}_i^{CHZ+(Lp)} k_{ij} \dot{u}_j^{CHZ+(Lp)} \mathrm{d}\left(S^{CHZ+(Lp)}\right) &= \left\{\delta\dot{\boldsymbol{u}}^{(1\sim4)}\right\}^T \left[K^{CHZ+(Lp)}\right] \left\{\dot{\boldsymbol{u}}^{(1\sim4)}\right\} \\ &= \left\{\delta\dot{\boldsymbol{u}}^{(1\sim4)}\right\}^T \int_{S^{CHZ+}} [\boldsymbol{N}]^T [\boldsymbol{k}][\boldsymbol{N}] \mathrm{d}\left(S^{CHZ+(Lp)}\right) \left\{\dot{\boldsymbol{u}}^{(1\sim4)}\right\} \end{aligned} \tag{71}$$

The other terms are expressed in the same manner, as:

$$\begin{aligned} \int_{S^{CHZ+}} \delta\dot{u}_i^{CHZ+(Lp)} k_{ij} \dot{u}_j^{CHZ-(Lp)} \mathrm{d}\left(S^{CHZ+(Lp)}\right) &= \left\{\delta\dot{\boldsymbol{u}}^{(1\sim4)}\right\}^T \left[K^{CHZ+(Lp)}\right] \left\{\dot{\boldsymbol{u}}^{(5\sim8)}\right\} \\ &= \left\{\delta\dot{\boldsymbol{u}}^{(1\sim4)}\right\}^T \int_{S^{CHZ+}} [\boldsymbol{N}]^T [\boldsymbol{k}][\boldsymbol{N}] \mathrm{d}\left(S^{CHZ+(Lp)}\right) \left\{\dot{\boldsymbol{u}}^{(5\sim8)}\right\} \end{aligned} \tag{72}$$

$$\begin{aligned}\int_{S^{CHZ+}} \delta\ddot{u}_i^{CHZ-(Lp)} k_{ij} \dot{u}_j^{CHZ+(Lp)} \mathrm{d}\left(S^{CHZ+(Lp)}\right) &= \left\{\delta\dot{\boldsymbol{u}}^{(5\sim8)}\right\}^T \left[K^{CHZ+(Lp)}\right]\left\{\dot{\boldsymbol{u}}^{(1\sim4)}\right\} \\ &= \left\{\delta\dot{\boldsymbol{u}}^{(5\sim8)}\right\}^T \int_{S^{CHZ+}} [\boldsymbol{N}]^T [\boldsymbol{k}][\boldsymbol{N}] \mathrm{d}\left(S^{CHZ+(Lp)}\right)\left\{\dot{\boldsymbol{u}}^{(1\sim4)}\right\}\end{aligned} \tag{73}$$

$$\begin{aligned}\int_{S^{CHZ+}} \delta\ddot{u}_i^{CHZ-(Lp)} k_{ij} \dot{u}_j^{CHZ+(Lp)} \mathrm{d}\left(S^{CHZ-(Lp)}\right) &= \left\{\delta\dot{\boldsymbol{u}}^{(5\sim8)}\right\}^T \left[K^{CHZ+(Lp)}\right]\left\{\dot{\boldsymbol{u}}^{(5\sim8)}\right\} \\ &= \left\{\delta\dot{\boldsymbol{u}}^{(5\sim8)}\right\}^T \int_{S^{CHZ+}} [\boldsymbol{N}]^T [\boldsymbol{k}][\boldsymbol{N}] \mathrm{d}\left(S^{CHZ+(Lp)}\right)\left\{\dot{\boldsymbol{u}}^{(5\sim8)}\right\}\end{aligned} \tag{74}$$

Thus, the term of the CHZ element can be written as its final form, as:

$$\begin{aligned}&\int_{S^{CHZ+}} \left(\delta\dot{u}_i^{CHZ+(Lp)} - \delta\dot{u}_i^{CHZ-(Lp)}\right) k_{ij} \left(\dot{u}_j^{CHZ+(Lp)} - \delta\dot{u}_j^{CHZ-(Lp)}\right) \mathrm{d}\left(S^{CHZ+(Lp)}\right) \\ &= \left\{\delta\dot{\boldsymbol{u}}^{(1\sim4)}\right\}^T \left[K^{CHZ+(Lp)}\right]\left\{\dot{\boldsymbol{u}}^{(1\sim4)}\right\} - \left\{\delta\dot{\boldsymbol{u}}^{(1\sim4)}\right\}^T \left[K^{CHZ+(Lp)}\right]\left\{\dot{\boldsymbol{u}}^{(5\sim8)}\right\} \\ &- \left\{\delta\dot{\boldsymbol{u}}^{(5\sim8)}\right\}^T \left[K^{CHZ+(Lp)}\right]\left\{\dot{\boldsymbol{u}}^{(1\sim4)}\right\} + \left\{\delta\dot{\boldsymbol{u}}^{(1\sim4)}\right\}^T \left[K^{CHZ+(Lp)}\right]\left\{\dot{\boldsymbol{u}}^{(1\sim4)}\right\} \\ &= \left\{\delta\dot{\boldsymbol{u}}^{(1\sim8)}\right\}^T \begin{bmatrix} K^{CHZ+(Lp)} & -K^{CHZ+(Lp)} \\ -K^{CHZ+(Lp)} & K^{CHZ+(Lp)} \end{bmatrix} \left\{\dot{\boldsymbol{u}}^{(1\sim8)}\right\}\end{aligned} \tag{75}$$

where

$$\left[K^{CHZ+(Lp)}\right] = \int_{S^{CHZ+}} [\boldsymbol{N}]^T [\boldsymbol{k}][\boldsymbol{N}] \mathrm{d}\left(S^{CHZ+(Lp)}\right) \tag{76}$$

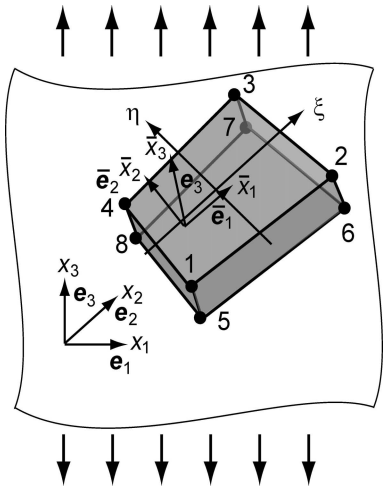

Figure 13 A schematic view of a cohesive zone element

4. Material damage evolution in particulate composite materials: damage constitutive laws

In this chapter, we discuss about the mechanical interactions between neighboring particles and the distribution and the evolution of material damage. We assume four kinds of materials; (1) the isotropic damage material and the separate dilatational/deviatoric damage material with the constant α being (2) 0.1, (3) 0.99 and (4) 10.0. For the separate dilatational/deviatoric damage model, the distributions of the dilatational and deviatoric damages are examined separately.

Matrix material is assumed to undergo the damage. The sources of damage evolutions are due to the nucleation and the growth of microvoids. The stress-strain curve of matrix material is postulated to be that of Kwon and Liu [10]. Although the uniaxial stress-strain curve of Kwon and Liu [10] was measured for a polymeric composite material, it is used to model matrix material in this investigation since there is no other available material behavior.

In this chapter, we discuss about (1) how the relationship between the effective stress-like parameters and the damage parameters are obtained, (2) the results of analyses for unit cell models are described.

4.1 Relationship between the effective stress-like parameters and the damage parameters.

4.1.1 The isotropic damage model

The damage evolution law of equation (9) has a scalar function $H(\bar{\tau},d)$ of $\bar{\tau}$ and d. $H(\bar{\tau},d)$ characterizes the damage evolution behavior and should be derived from a set of experimental data. In this section, how the scalar function $H(\bar{\tau},d)$ is determined is described.

First, we assume that we have a stress-strain curve which was measured in an experiment. Let us assume that we have a uniaxial stress-strain curve, as shown in Figure 14 Stress is expressed by:

$$\sigma = (1-d)E\varepsilon \tag{77}$$

Therefore, the damage parameter d is expressed by the stress and strain, as:

$$d = 1 - \frac{\sigma}{E\varepsilon} \tag{78}$$

The value of the effective stress-like parameter $\bar{\tau}$ can be written in terms of the uniaxial stress and strain, as:

$$\bar{\tau} = \sqrt{C_{ijk\ell}\varepsilon_{ij}\varepsilon_{k\ell}} = \sqrt{\sigma^{o}_{k\ell}\varepsilon_{k\ell}} = \sqrt{\frac{\sigma_{k\ell}}{1-d}\varepsilon_{k\ell}} = \sqrt{\frac{\sigma}{1-d}\varepsilon} = \sqrt{\sigma^{o}\varepsilon} = \sqrt{E\varepsilon^{2}} \tag{79}$$

Therefore, once the uniaxial stress-strain curve is given, relationship between the effective stress-like and the damage parameter can be obtained. In present investigation, a uniaxial stress-strain curve is approximated by a series of piecewise straight lines, as depicted in Figure 15. In Figure 15, points on the stress-strain curve (σ_1,ε_1), (σ_2,ε_2), (σ_3,ε_3), $\bullet\bullet\bullet$, (σ_i,ε_i), $(\sigma_{i+1},\varepsilon_{i+1})$, $\bullet\bullet\bullet$ connect straight line segments. From a set of data (σ_1,ε_1), (σ_2,ε_2), (σ_3,ε_3), $\bullet\bullet\bullet$, (σ_i,ε_i), $(\sigma_{i+1},\varepsilon_{i+1})$, $\bullet\bullet\bullet$, we can compute $(\bar{\tau}_1,d_1)$, $(\bar{\tau}_2,d_2)$, $(\bar{\tau}_3,d_3)$, $\bullet\bullet\bullet$, $(\bar{\tau}_i,d_i)$, $(\bar{\tau}_{i+1},d_{i+1})$, $\bullet\bullet\bullet$ by using equations (78) and (60). Thus, the relationship between $\bar{\tau}$ and d is also approximated by a series of piecewise straight lines. The function $H(\bar{\tau},d)$ which governs the damage evolution law of equation (20) is approximated by:

$$H(\bar{\tau},d) = \frac{\dot{d}}{\dot{\bar{\tau}}} \approx \frac{d_{i+1}-d_i}{\bar{\tau}_{i+1}-\bar{\tau}_i} \qquad (d_i < d < d_{i+1}, \bar{\tau}_i < \bar{\tau} < \bar{\tau}_{i+1}) \tag{80}$$

The function $H(\bar{\tau},d)$ whose value is determined by equation (80) is used in the stress-strain relationship of equation (21).

We then extract a series of data points (σ_1,ε_1), (σ_2,ε_2), (σ_3,ε_3), $\bullet\bullet\bullet$, (σ_7,ε_7), from the experimental stress-strain curve of Kwon and Liu [10], as shown in Figure 16. As an example, the relationship between the uniaxial strain and the damage parameter for the case of isotropic damage is depicted in Figure 17. Thus, the uniaxial stress-strain curve is reconstructed by a series of linear approximations, as shown in Figure 18.

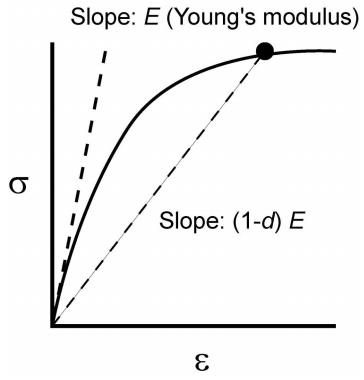

Fig. 14 Uniaxial stress-strain curve

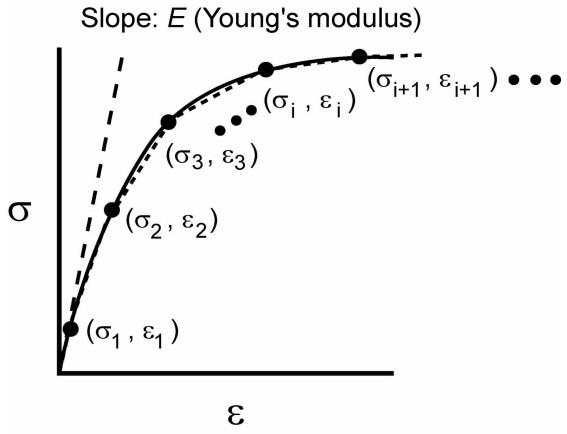

Fig. 15 Piecewise linear approximation for uniaxial stress-strain curve

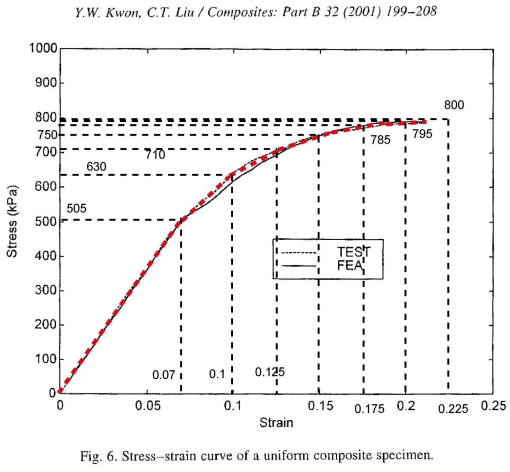

Fig. 6. Stress–strain curve of a uniform composite specimen.

Figure 16 Uniaxial stress-strain curve of polymeric particulate composite material that was given in Kwon and Liu [10]

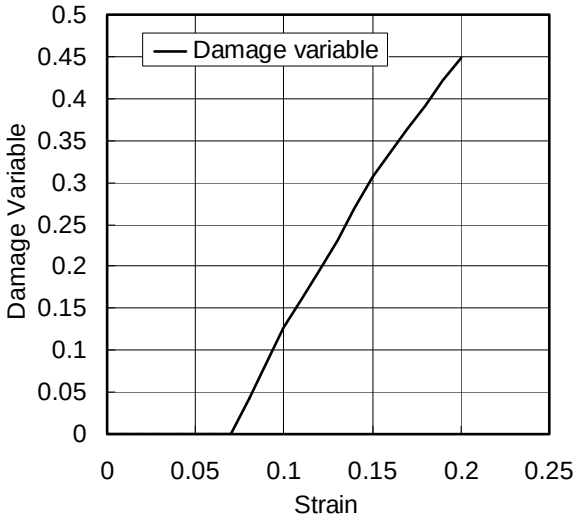

Figure 17 Relationship between the strain and the damage parameter for the isotropic damage constitutive model, which was extracted from the stress-strain curve of Figure 16.

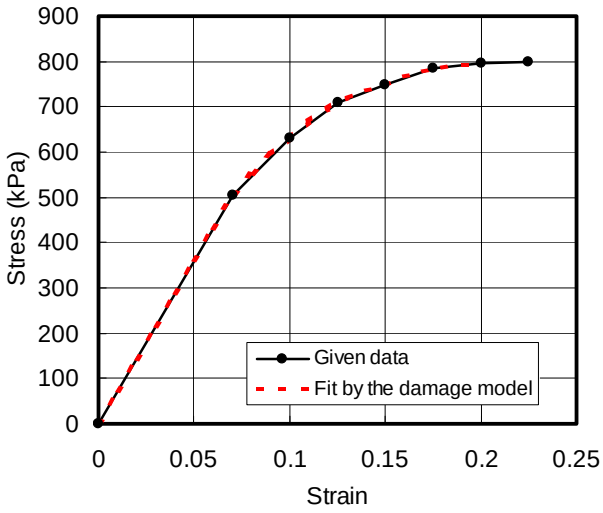

Figure 18 Uniaxial stress-strain curve that was reconstructed after the relationship between the effective stress-like and the damage parameters is established by the proposed procedures.

4.1.2 The separate Isotropic/deviatoric damage model

In this section, the damage evolution law for the separate isotropic/deviatoric damage

model is dealt with. As seen in equations (28) and (29), there are two different damage evolution laws and two damage variables $H_V(\bar{\tau}_V, d_V)$ and $H_D(\bar{\tau}_D, d_D)$. In order to fully determine $H_V(\bar{\tau}_V, d_V)$ and $H_D(\bar{\tau}_D, d_D)$, we need at least two sets of stress-strain curves. When only one stress-strain curve is available, we need to introduce at least one additional condition.

We assume that a uniaxial stress-strain curve, as shown in Figure 15 or 16 is available. As an additional condition to uniquely determine the damage evolution law, we postulate that the ratio (d_V/d_D) between the dilatational and deviatoric damage parameters remains to be the same during the uniaxial deformation. We write:

$$d_D = \alpha d_V \tag{81}$$

Here, α is a positive constant ($0 \le \alpha \le \infty$). When α equals zero, only the dilatational damage is present. When $\alpha = 1$, the magnitudes of dilatational and deviatoric parts equal each other and, therefore, this case is very similar to that of the isotropic damage. When α is infinitely large, the dilatational damage parameter d_V is zero. Therefore, material undergoes deviatoric damage only.

We assume uniaxial deformation in x_1 direction. We can write the following statements.

$$\begin{aligned} &\sigma_{11} \neq 0 \quad (\text{unknown}); \quad \sigma_{22} = \sigma_{33} = \sigma_{12} = \sigma_{23} = \sigma_{31} = 0 \quad (\text{known}) \\ &\varepsilon_{11} \neq 0, \quad \varepsilon_{12} = \varepsilon_{23} = \varepsilon_{31} = 0 \quad (\text{known}); \quad \varepsilon_{22} = \varepsilon_{33} \quad (\text{unknown}) \end{aligned} \tag{82}$$

Therefore, by substituting equations (62) and (63) in equation (82), we have:

$$\begin{aligned} \sigma_{11} &= (1-d_V)K(\varepsilon_{11}+\varepsilon_{22}+\varepsilon_{33}) + \frac{2}{3}(1-\alpha d_V)\mu(2\varepsilon_{11}-\varepsilon_{22}-\varepsilon_{33}) \\ \sigma_{22} &= (1-d_V)K(\varepsilon_{11}+\varepsilon_{22}+\varepsilon_{33}) + \frac{2}{3}(1-\alpha d_V)\mu(2\varepsilon_{22}-\varepsilon_{33}-\varepsilon_{11}) \\ \sigma_{11} &= (1-d_V)K(\varepsilon_{11}+\varepsilon_{22}+\varepsilon_{33}) + \frac{2}{3}(1-\alpha d_V)\mu(2\varepsilon_{33}-\varepsilon_{11}-\varepsilon_{22}) \end{aligned} \tag{83}$$

From the second and the third of equation (83) and $\varepsilon_{22} = \varepsilon_{33}$, one can obtain:

$$0 = (1-d_V)K(\varepsilon_{11}+\varepsilon_{22}+\varepsilon_{33}) + \frac{2}{3}(1-\alpha d_V)\mu(\varepsilon_{11}-\varepsilon_{22}) \tag{84}$$

The first of equation (83) and equation (84) lead to:

$$\varepsilon_{22} = \frac{-\sigma_{11}}{2(1-\alpha d_V)\mu} + \varepsilon_{11} \tag{85}$$

By substituting equation (85) in the first of equation (83), we can establish a relationship between σ_{11} and ε_{11}, as:

$$3(1-\alpha d_V)(1-d_V)\mu K\varepsilon_{11} - \left\{\frac{1}{3}(1-\alpha d_V)\mu + (1-d_V)K\right\}\sigma_{11} = 0 \tag{86}$$

By rearranging equation (86), we can establish:

$$\alpha d_V^2 + \left\{\frac{\alpha\mu + 3K}{9\mu K}\frac{\sigma_{11}}{\varepsilon_{11}} - (1+\alpha)\right\}d_V + \left(1 - \frac{\sigma_{11}}{E\varepsilon_{11}}\right) = 0 \tag{87}$$

Therefore, for a give set of variables σ_{11}, ε_{11} and α, we can solve for d_V.
Two special cases ($\alpha = 0$ and $\alpha = 1$) are presented first. When $\alpha = 0$, we have:

$$0 \cdot d_V^2 + \left\{\frac{0\cdot\mu + 3K}{9\mu K}\frac{\sigma_{11}}{\varepsilon_{11}} - (1+0)\right\}d_V + \left(1 - \frac{\sigma_{11}}{E\varepsilon_{11}}\right) = 0 \tag{88}$$

and,

$$d_V = 1 - \frac{\sigma_{11}}{3K\left(3\varepsilon_{11} - \frac{\sigma_{11}}{\mu}\right)} \qquad (\alpha = 0) \tag{89}$$

When $\alpha = 1$, we have:

$$d_V^2 + \left\{\frac{\mu + 3K}{9\mu K}\frac{\sigma_{11}}{\varepsilon_{11}} - 2\right\}d_V + \left(1 - \frac{\sigma_{11}}{E\varepsilon_{11}}\right) = 0 \tag{90}$$

and,

$$d_V = 1 - \frac{\sigma_{11}}{E\varepsilon_{11}} \qquad (\alpha = 0) \tag{91}$$

In is noted that there are two solutions that satisfy equation (90) and they are $d_V = 1 - \frac{\sigma_{11}}{E\varepsilon_{11}}$ and $d_V = 1$. The second one takes a constant value and, therefore, is not a feasible solution. For more general case ($\alpha \neq 0,1$), we solve equation (87) for d_V, by letting:

$$\alpha d_V^2 + A d_V + B = 0 \tag{92}$$

$$A = \frac{\alpha\mu + 3K}{9\mu K}\frac{\sigma_{11}}{\varepsilon_{11}} - (1+\alpha) \qquad \text{and} \quad B = 1 - \frac{\sigma_{11}}{E\varepsilon_{11}} \tag{93}$$

Therefore, the value d_V is determined to be:

$$d_V = \frac{-A \pm \sqrt{A^2 - 4\alpha B}}{2\alpha} \tag{94}$$

In equation (94), the sign associated with $\sqrt{A^2 - 4\alpha B}$ needs to be determined. To determine the sign, we check a special case ($\alpha = 1$). By letting $\alpha = 1$, in equation (94), we have:

$$d_V = \frac{1}{2}\left\{-\left(\frac{\sigma_{11}}{E\varepsilon_{11}} - 2\right) \pm \frac{\sigma_{11}}{E\varepsilon_{11}}\right\} \tag{95}$$

When we take the positive sign, equation (95) results in:

$$d_V = \frac{1}{2}\left\{-\left(\frac{\sigma_{11}}{E\varepsilon_{11}} - 2\right) + \frac{\sigma_{11}}{E\varepsilon_{11}}\right\} = 1 \tag{96}$$

This is a constant value ($d_V = 1$) and, therefore, is inappropriate. When the negative sign is assumed, we obtain:

$$d_V = \frac{1}{2}\left\{-\left(\frac{\sigma_{11}}{E\varepsilon_{11}} - 2\right) - \frac{\sigma_{11}}{E\varepsilon_{11}}\right\} = 1 - \frac{\sigma_{11}}{E\varepsilon_{11}} \tag{97}$$

This result is the same as the case of isotropic damage material (equation (78)). Therefore, we choose the negative sign in equation (94).

$$d_V = \frac{-A - \sqrt{A^2 - 4\alpha B}}{2\alpha} \tag{98}$$

Thus, the deviatoric damage parameter d_D is also determined to be:

$$d_D = \alpha d_V = \alpha \frac{-A - \sqrt{A^2 - 4\alpha B}}{2\alpha} \tag{99}$$

Once uniaxial stress-strain curve as depicted in Figure 14 is given, we correct a series of points $(\sigma_1, \varepsilon_1)$, $(\sigma_2, \varepsilon_2)$, $(\sigma_3, \varepsilon_3)$, $\bullet\bullet\bullet$, $(\sigma_i, \varepsilon_i)$, $(\sigma_{i+1}, \varepsilon_{i+1})$, $\bullet\bullet\bullet$, on the curve, as shown in Figure 15. Damage parameters ($d_V|_i$ and $d_D|_i$) corresponding to the stress and strain $(\sigma_i, \varepsilon_i)$ are obtained. Thus, by using equations (82) and (83), unknown strains ε_{22} and ε_{33} ($\varepsilon_{22} = \varepsilon_{33}$) are derived. Therefore, we can compute the effective stress-like terms $\bar{\tau}_V \left(= \sqrt{K}\varepsilon_{kk}\right)$ and $\bar{\tau}_D \left(= \sqrt{\mu \varepsilon'_{ij} \varepsilon'_{ij}}\right)$. Thus, we have a series of data $\left(d_V|_1, d_D|_1, \bar{\tau}_V|_1, \bar{\tau}_D|_1\right)$, $\left(d_V|_2, d_D|_2, \bar{\tau}_V|_2, \bar{\tau}_D|_2\right)$, $\left(d_V|_3, d_D|_3, \bar{\tau}_V|_3, \bar{\tau}_D|_3\right)$, $\bullet\bullet\bullet$, $\left(d_V|_i, d_D|_i, \bar{\tau}_V|_i, \bar{\tau}_D|_i\right)$, $\left(d_V|_{i+1}, d_D|_{i+1}, \bar{\tau}_V|_{i+1}, \bar{\tau}_D|_{i+1}\right)$, $\bullet\bullet\bullet$. The scalar functions, $H_V(\bar{\tau}_V, d_V)$ and $H_D(\bar{\tau}_D, d_D)$ are derived to be:

$$\begin{aligned} H_V(\bar{\tau}_V, d_V) &= \frac{\dot{d}_V}{\dot{\bar{\tau}}_V} \approx \frac{d_V|_{i+1} - d_V|_i}{\bar{\tau}_V|_{i+1} - \bar{\tau}_V|_i} \qquad \left(d_V|_i < d_V < d_V|_{i+1}, \bar{\tau}_V|_i < \bar{\tau}_V < \bar{\tau}_V|_{i+1}\right) \\ H_D(\bar{\tau}_D, d_D) &= \frac{\dot{d}_D}{\dot{\bar{\tau}}_D} \approx \frac{d_D|_{i+1} - d_D|_i}{\bar{\tau}_D|_{i+1} - \bar{\tau}_D|_i} \qquad \left(d_D|_i < d_D < d_D|_{i+1}, \bar{\tau}_D|_i < \bar{\tau}_D < \bar{\tau}_D|_{i+1}\right) \end{aligned} \tag{100}$$

5. Material damage evolution in particulate composite materials-cohesive zone model (dewetting between the particles and matrix material)

5.1 Material damage evolution in matrix material under the influences of mechanical interactions of particles-1 (Four particle model without ambient pressure)

In this section, we try to present how the damage zone develop when particulate composite materials are loaded. First, we consider a simple problem such that a block containing four particles is subject to tension, with or without ambient pressure.

In Figure 19, a model that contains four particles is presented. The finite element models for the s-FEM analysis are also illustrated in Figure 19. As presented in previous chapter, the stress-strain curve of Kwon and Liu [10] is postulated and the relationship between the effective stress-like parameters and the damage parameters are obtained. From the results of this simple problem, we can clarify the influences of particle arrangements and of ambient pressure to the evolution of matrix damage.

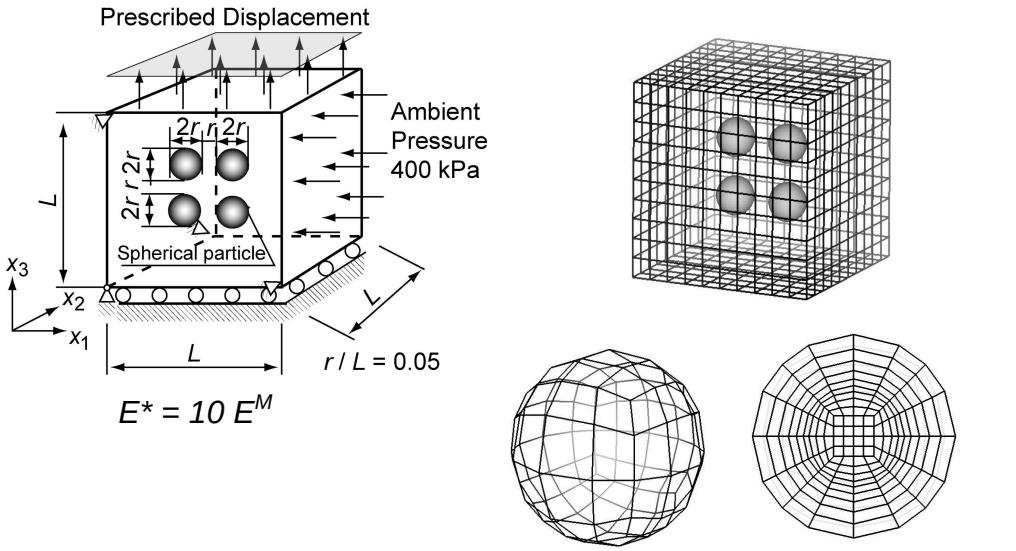

Figure 19 The problem of four particles with and without the ambient pressure

5.1.1 Isotropic damage material without ambient pressure

The distributions of stresses and damage parameter are presented in Figure 20, for the levels of overall strain $\bar{\varepsilon}$ being 0.0632 and 0.1. It is seen that, for $\bar{\varepsilon} = 0.0632$, both tensile and transverse stresses concentrate at the top and bottom of the particles. The magnitude of the concentrations seem to be slightly severer in the gaps between the particles than the other locations. Both tensile and transverse stresses are positive, resulsting in a large value of hydrostatic stress. Dmage zones start to develop at the top and bottom of the particles. In the gaps between the particles, the damage parameter is slightly larger than the other locations. That is very similar to the case of stresses.

For $\bar{\varepsilon} = 0.1$, the major trends are similar to the case of $\bar{\varepsilon} = 0.0632$. However, material damage takes place almost throughout the region of matrix material.

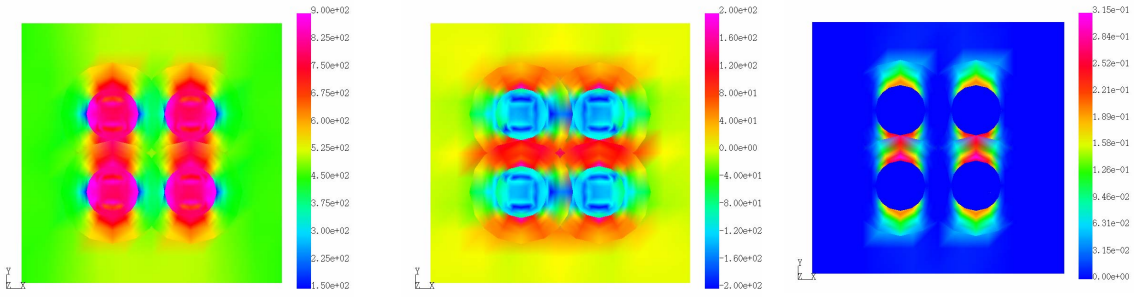

(a-1) Tensile stress (a-2) Transverse stress (a-3) Damage parameter

(a) $\bar{\varepsilon} = 0.0632$

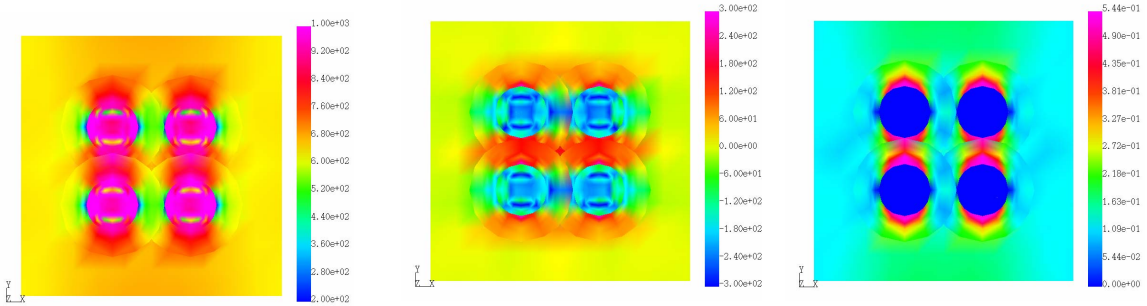

(b-1) Tensile stress (b-2) Transverse stress (b-3) Damage parameter

(b) $\bar{\varepsilon} = 0.1$

Figure 20 The distributions of the tensile and transverse stresses and the damage parameter for the case of isotropic damage without ambient pressure

5.1.2 Separate dilatational/deviatoric damage material with α = 0.1 and without ambient pressure

In the case of the separate dilatational/deviatoric damage model, the dilatational damage is set to dominate the other. In Figure 21, it is seen that, for $\bar{\varepsilon} = 0.0632$, the distributions of the tensile and transverse stresses are similar to those of the isotropic damage case. The distributions of the transverse stress look differently. That is because the ranges are different. The dilatational and deviatoric damage zones develop at the top and bottom of the particles. They connect the particles in vertical direction. No damage develops in horizontal directions from the particles. As expected, the dilatational damage parameter is much larger than the deviatoric one.

When the level of overall strain $\bar{\varepsilon}$ increases to 0.1, the damage zones enlarge and the most of part of matrix material suffer from the material damages. The dilatational damage parameter is much larger than the deviatoric one. The particles constrain the deformation of matrix material and the damage variables at both the sides of the particles are almost zero.

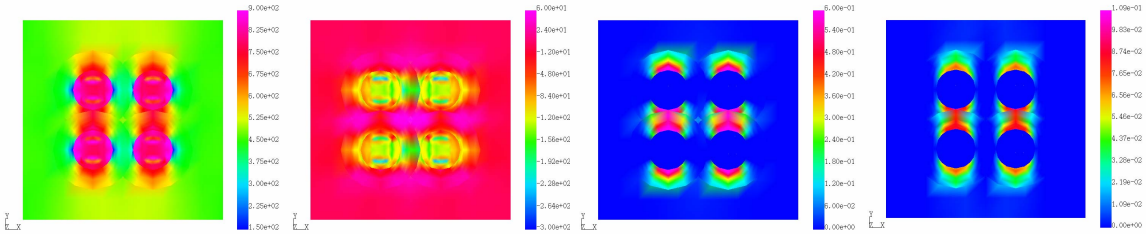

(a-1) Tensile stress (a-2) Transverse stress (a-3) Dilatational damage parameter (a-4) Deviatoric damage parameter

(a) $\bar{\varepsilon} = 0.0632$

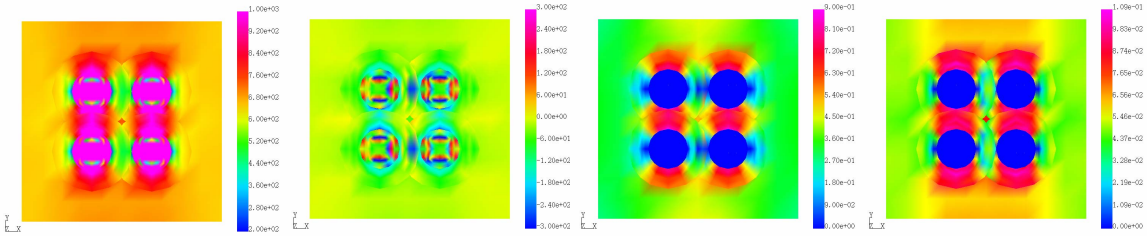

(b-1) Tensile stress (b-2) Transverse stress (b-3) Dilatational damage parameter (b-4) Deviatoric damage parameter

(b) $\bar{\varepsilon} = 0.1$

Figure 21 The distributions of the tensile and transverse stresses and the damage parameter for the case of the separate dilatational/deviatoric damage model with $\alpha = 0.1$ and without ambient pressure

5.1.3 Separate dilatational/deviatoric damage material with α = 0.99 and without ambient pressure

In this case, parameter α is set to be 0.99. The distributions of tensile and transverse stresses and the dilatational and deviatoric damage parameters are depicted in Figure 22. The distributions of the stresses are similar to afore mentioned cases. Material damages develop at the top and bottom of the particles where stresses are large. As shown in Figures 22 (a-3), (a-4), (b-3) and (b-4), the levels of the dilatational and deviatoric damage parameters are similar. Their patterns of distributions are slightly different. The dilatational damage variable at the sides of particles is almost zero and such regions connect the particles in horizontal directions.

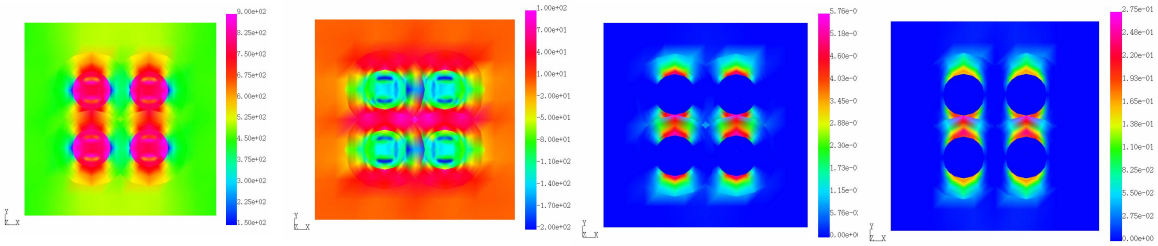

(a-1) Tensile stress (a-2) Transverse stress (a-3) Dilatational damage parameter (a-4) Deviatoric damage parameter

(a) $\bar{\varepsilon} = 0.0632$

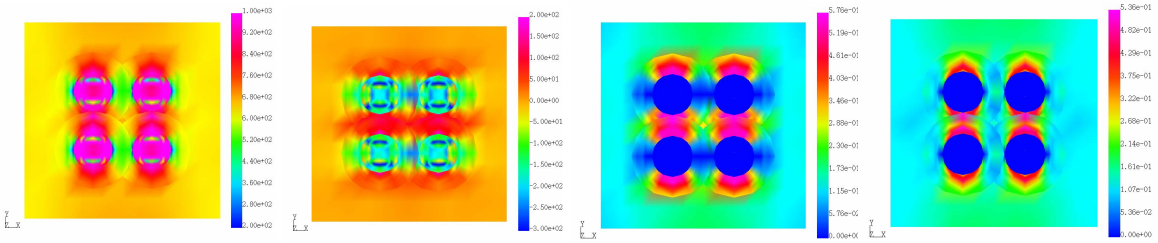

(b-1) Tensile stress (b-2) Transverse stress (b-3) Dilatational damage parameter (b-4) Deviatoric damage parameter

(b) $\bar{\varepsilon} = 0.1$

Figure 22 The distributions of the tensile and transverse stresses and the damage parameter for the case of the separate dilatational/deviatoric damage model with $\alpha = 0.99$ and without ambient pressure

5.1.4 Separate dilatational/deviatoric damage material with α = 10.0 and without ambient pressure

In this case, the parameter α is set to be 10. It is assumed that the deviatoric damage mode dominates the dilatational one. In Figure 23, the distributions of the stresses and the damage parameters are shown.

The distributions of stresses are similar to afore mentioned cases. The level of the deviatoric damage parameter is much larger than the dilatational one.

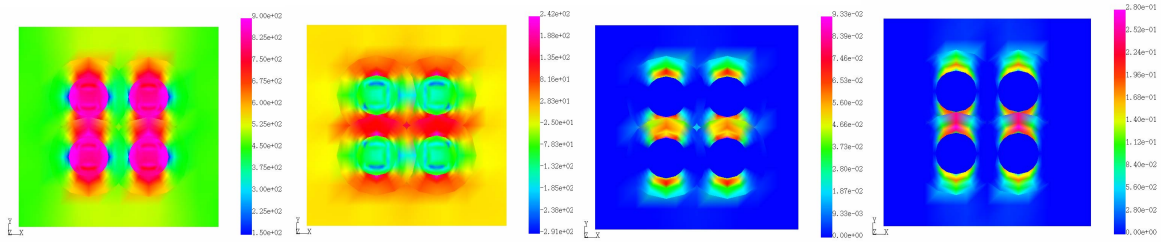

(a-1) Tensile stress (a-2) Transverse stress (a-3) Dilatational damage parameter (a-4) Deviatoric damage parameter

(a) $\bar{\varepsilon} = 0.0632$

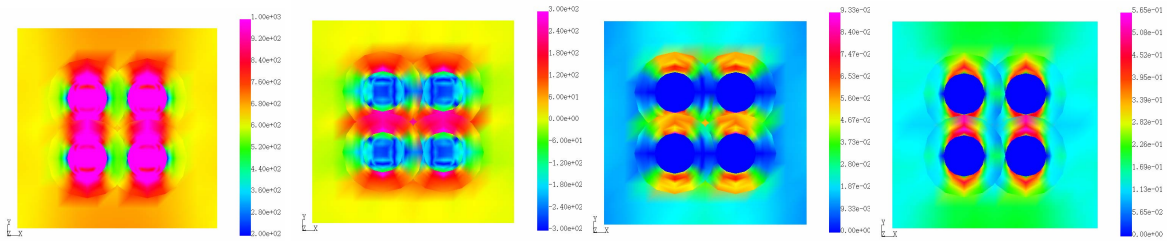

(b-1) Tensile stress (b-2) Transverse stress (b-3) Dilatational damage parameter (b-4) Deviatoric damage parameter

(b) $\bar{\varepsilon} = 0.1$

Figure 23 The distributions of the tensile and transverse stresses and the damage parameter for the case of the separate dilatational/deviatoric damage model with $\alpha = 10.0$ and without ambient pressure

5.1.5 Summary: Separate dilatational/deviatoric damage material with α = 0.1, 0.99 and 10.0, and without ambient pressure

The distributions of the tensile and transverse stresses and the dilatational and deviatoric damage parameters are described in section 5.1.1~5.1.4. The stresses are large at the top and bottom of the particles. The regions of high stress connect the particles in the vertical direction. At the sides of the particles, the particles constrain matrix material from deformation. Therefore, the damage parameters are small at the sides of the particles. The overall trends of distributions of the dilatational and deviatoric damage parameters are very similar. Therefore, it is summarized that the choice of constitutive models (the isotropic and the separate dilatational/deviatoric damage models with different constant α) does not make much difference in the results when no ambient pressure loading is applied to the block.

5.2 Material damage evolution in matrix material under the influences of mechanical interactions of particles-2 (Four particle model with ambient pressure)

In this section, the same four particle problems are solved with ambient pressure that is applied as distributed force from the sides of the block. The ambient pressure is 400kPa.

Results (the distributions of tensile and transverse stresses and the dilatational and deviatoric damage parameters) are visualized for overall tensile strain $\bar{\varepsilon}$ being 0.1 and 0.135. Since the ambient pressure is applied, Poisson's ratio effect produces negative tensile stress. Thus, overall tensile strain $\bar{\varepsilon}$ is set to be 0.1 or 0.135 so that the tensile stress in the block is almost the same as the cases of previous section (without ambient pressure).

5.2.1 Isotropic damage material with ambient pressure

In Figure 24, the distributions of tensile and transverse stresses and the isotropic damage parameter are depicted. Major trends in the distributions of tensile stress are similar to those without the ambient pressure. Also, major trends in the distributions of transverse stress are also analogous to those without the ambient pressure, except for that the value of stress is about -400 kPa at distant points from the particles whereas it is about zero for the case without the ambient pressure.

The distributions of the isotropic damage parameter are quite different from those without the ambient pressure. When the block is subject to tension without the ambient pressure, the damage zones develop at the top and bottom of the particles and do not appear at the sides of the particles. However, with the ambient pressure, the damage zones develop at the sides of the particles. The concentration of negative stress due to ambient pressure occurs at the sides of the particles. That is why the damage zones develop at the sides of the particles.

Development of damage zone due to the growth and nucleation of microvoids under negative stress are not likely to occur. Therefore, the use of isotropic damage constitutive model may not be suitable for present investigation.

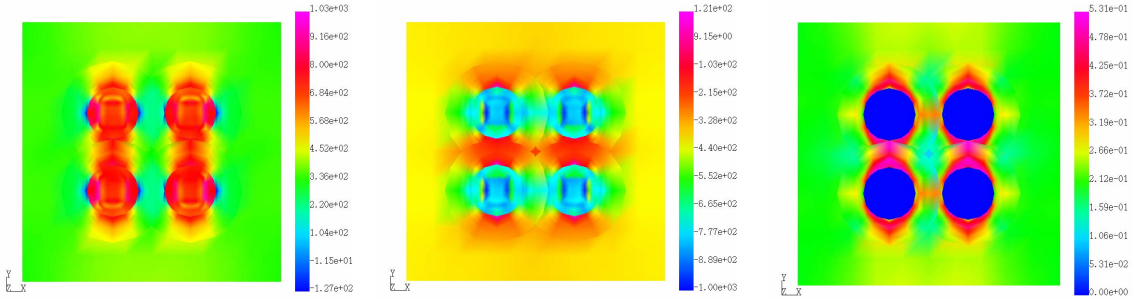

(a-1) Tensile stress (a-2) Transverse stress (a-3) Damage parameter

(a) $\bar{\varepsilon} = 0.1$

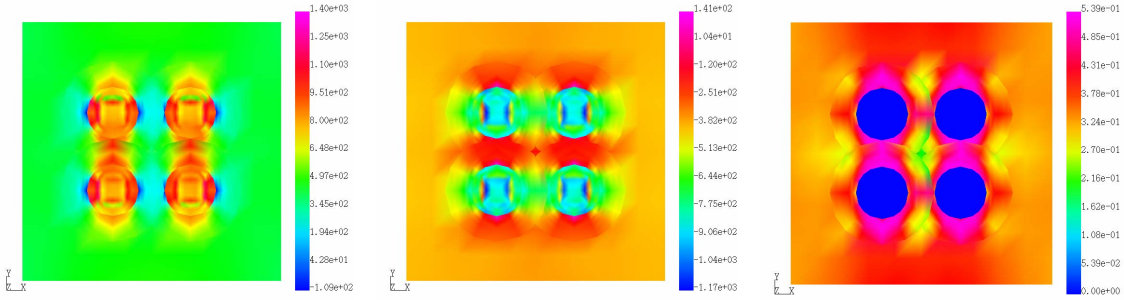

(b-1) Tensile stress (b-2) Transverse stress (b-3) Damage parameter

(b) $\bar{\varepsilon} = 0.135$

Figure 24 The distributions of the tensile and transverse stresses and the damage parameter for the case of isotropic damage with ambient pressure

5.2.2 Separate dilatational/deviatoric damage material with α = 0.1 and with ambient pressure

The distributions of tensile and transverse stresses and the dilatational and deviatoric damage parameters are depicted in Figure 25. The distributions of the stresses are similar to those of the isotropic damage constitutive law. The distributions of the damage parameters are quite interesting. The dilatational damage parameter is very small compared with the case without the ambient pressure. The distributions of deviatoric damage parameter are almost uniform within matrix material. The level of the deviatoric damage parameter is small.

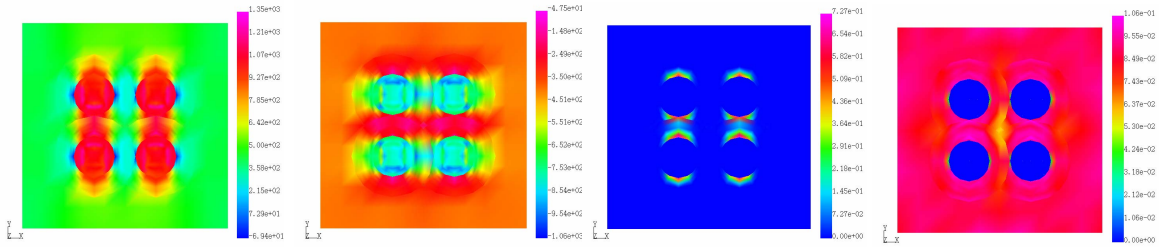

(a-1) Tensile stress (a-2) Transverse stress (a-3) Dilatational damage parameter (a-4) Deviatoric damage parameter

(a) $\bar{\varepsilon} = 0.1$

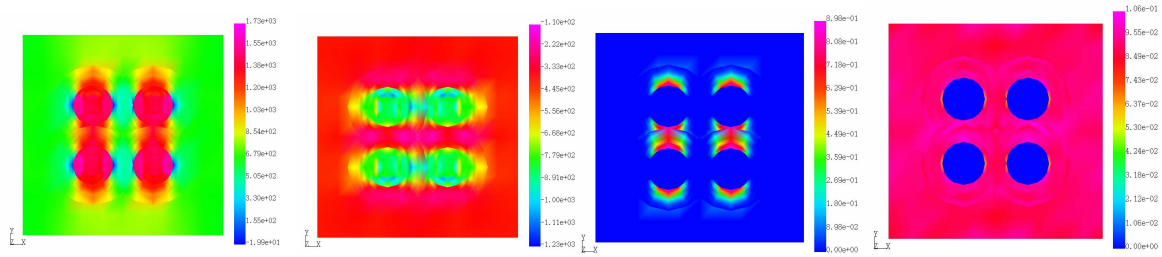

(b-1) Tensile stress (b-2) Transverse stress (b-3) Dilatational damage parameter (b-4) Deviatoric damage parameter

(b) $\bar{\varepsilon} = 0.135$

Figure 25 The distributions of the tensile and transverse stresses and the damage parameter for the case of the separate dilatational/deviatoric damage model with $\alpha = 0.1$ and with the ambient pressure

5.2.3 Separate dilatational/deviatoric damage material with α = 0.99 and with ambient pressure

The distributions of tensile and transverse stresses and the dilatational and deviatoric damage parameters are depicted in Figure 26. It is seen that the dilatational damage parameter is much smaller than the deviatoric one. The distributions of the deviatoric damage parameter are analogous to the cases of the isotropic damage constitutive law with the ambient pressure. This implies that the development of damage in the case of the isotropic damage law is governed by the deviatoric stresses.

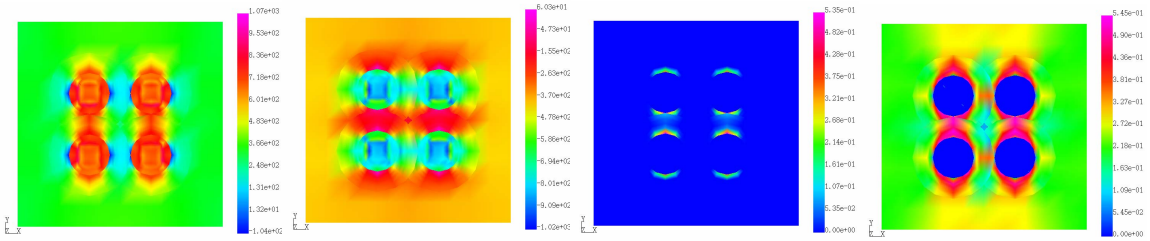

(a-1) Tensile stress (a-2) Transverse stress (a-3) Dilatational damage parameter (a-4) Deviatoric damage parameter

(a) $\bar{\varepsilon} = 0.1$

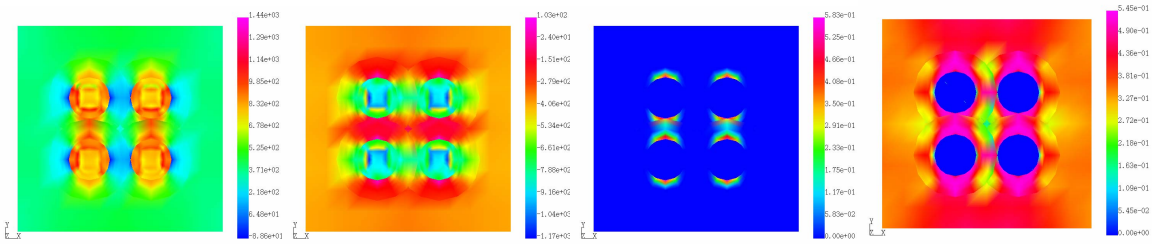

(b-1) Tensile stress (b-2) Transverse stress (b-3) Dilatational damage parameter (b-4) Deviatoric damage parameter

(b) $\bar{\varepsilon} = 0.135$

Figure 26 The distributions of the tensile and transverse stresses and the damage parameter for the case of the separate dilatational/deviatoric damage model with $\alpha = 0.99$ and with the ambient pressure

5.2.4 Separate dilatational/deviatoric damage material with α = 10.0 and with ambient pressure

The distributions of tensile and transverse stresses and the dilatational and deviatoric damage parameters are depicted in Figure 27. The distributions of the stresses are similar to those of the isotropic and the separate dilatational/deviatoric damage model with the other values of parameter α. As the parameter α is set to be 10.0, the dilatational damage parameter is much smaller than the deviatoric one. The distributions of the deviatoric damage parameter look similar to previous cases that are of the isotropic and the dilatational/deviatoric damage with $\alpha = 0.1$ and $\alpha = 0.99$.

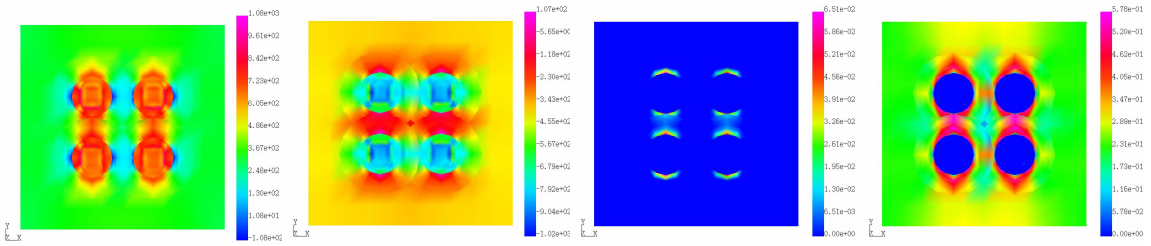

(a-1) Tensile stress (a-2) Transverse stress (a-3) Dilatational damage parameter (a-4) Deviatoric damage parameter

(a) $\bar{\varepsilon} = 0.1$

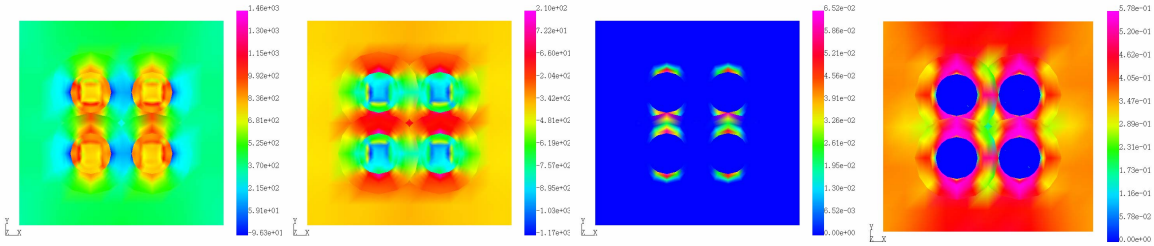

(b-1) Tensile stress (b-2) Transverse stress (b-3) Dilatational damage parameter (b-4) Deviatoric damage parameter

(b) $\bar{\varepsilon} = 0.135$

Figure 27 The distributions of the tensile and transverse stresses and the damage parameter for the case of the separate dilatational/deviatoric damage model with $\alpha = 10.0$ and with the ambient pressure

5.2.5 Summary: Separate dilatational/deviatoric damage material with α = 0.1, 0.99 and 10.0, and with the ambient pressure

Results with the ambient pressure revealed that when the isotropic damage model is used, the progressive material damage occurs even under negative hydrostatic stress. This contradicts with our basic postulation that the damage in matrix material is due to the growth and nucleation of microvoids. These should not be sensitive to the deviatoric stresses. Therefore, it is plausible to use the separate dilatational/deviatoric damage model with a small value of constant α.

From present sets of analyses we are unable to suggest the most suitable value for α.

5.3 Material damage evolution in matrix material under the influences of mechanical interactions of particles-3 (Nine randomly distributed particle model with and without ambient pressure)

Following the four particle problems, we solved a problem with nine randomly distributed particles. The problem configuration is depicted in Figure 28. Again, we adopt the isotropic damage model and the separate dilatational/deviatoric damage constitutive model with $\alpha = 0.1$, $\alpha = 0.99$ and $\alpha = 10.0$. Analyses are carried out with and without the ambient pressure.

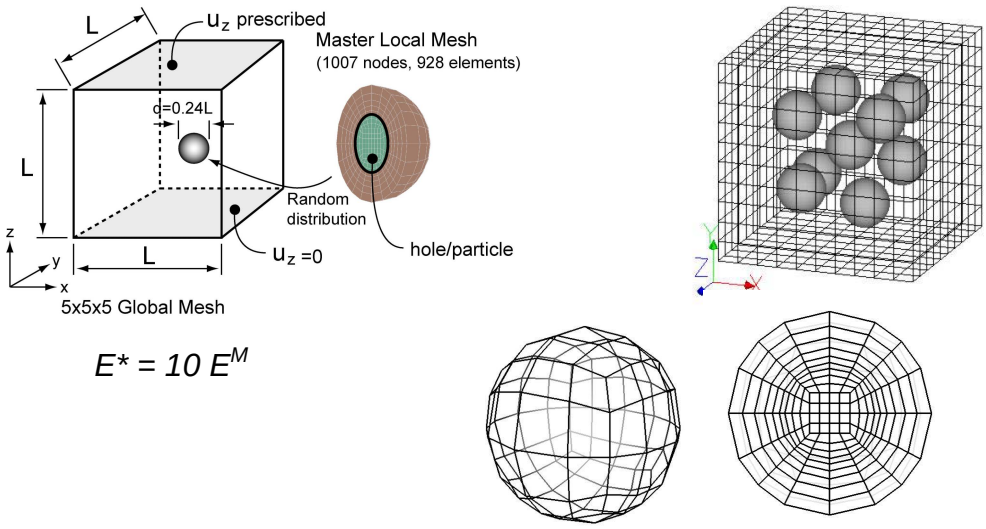

Figure 28 The problem of none randomly distributed particles with and without the ambient pressure

5.3.1 Isotropic damage material without ambient pressure (Nine randomly distributed particle model)

The distributions of tensile and transverse stresses and the damage parameter are presented in Figure 29. Trends are similar to the case of four regularly distributed particles.

It is seen in Figures 29 (a-3) and (b-3) that the zone of large value of the damage parameter connects the particles when they are close to each other. The stresses concentrate at the top and bottom of the particles. The transverse stress at the sides of the particles is negative and the zones of negative stress connect the particles when the distances between particles are small.

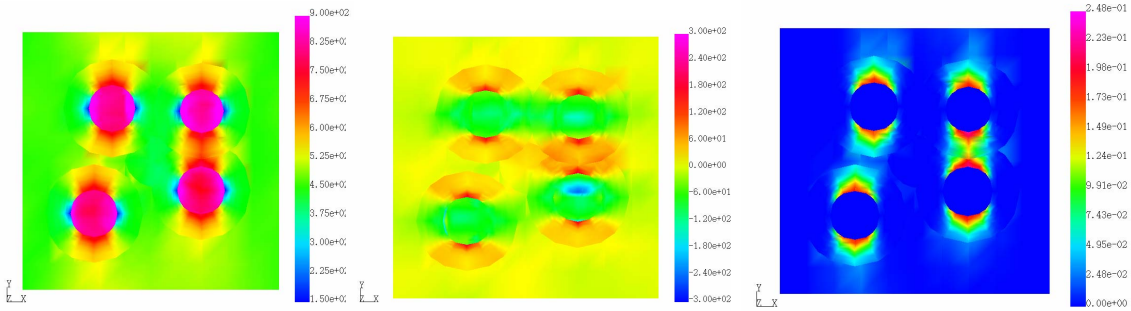

(a-1) Tensile stress (a-2) Transverse stress (a-3) Damage parameter

(a) $\bar{\varepsilon} = 0.0632$

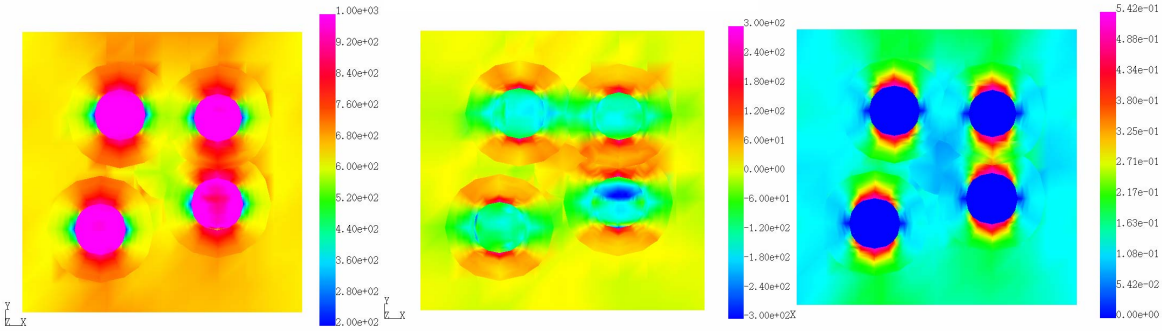

(b-1) Tensile stress (b-2) Transverse stress (b-3) Damage parameter

(b) $\bar{\varepsilon} = 0.1$

Figure 29 The distributions of the tensile and transverse stresses and the damage parameter for the case of isotropic damage without ambient pressure (Nine randomly distributed particle model)

5.3.2 Separate dilatational/deviatoric damage material with α = 0.1 and without ambient pressure (Nine randomly distributed particle model)

The distributions of tensile and transverse stresses and the dilatational and deviatoric damage parameters are presented in Figure 30. The overall trends are similar to that of four regularly distributed particle case. Again, the concentration of the transverse stress is not very clear.

The value of the dilatational damage parameter is much larger than that of the deviatoric one.

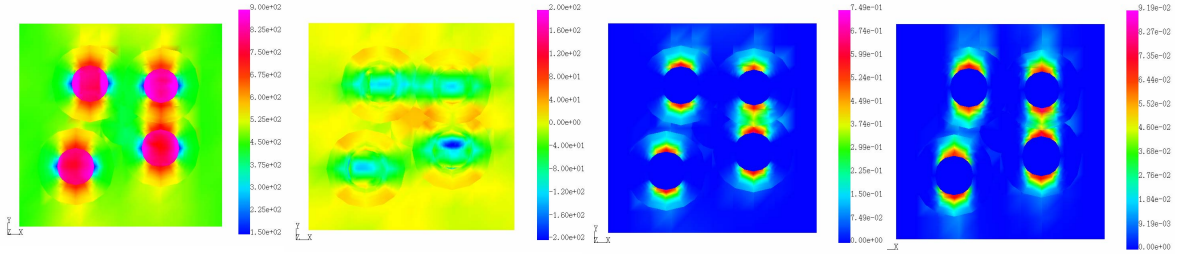

(a-1) Tensile stress (a-2) Transverse stress (a-3) Dilatational damage parameter (a-4) Deviatoric damage parameter

(a) $\bar{\varepsilon} = 0.0632$

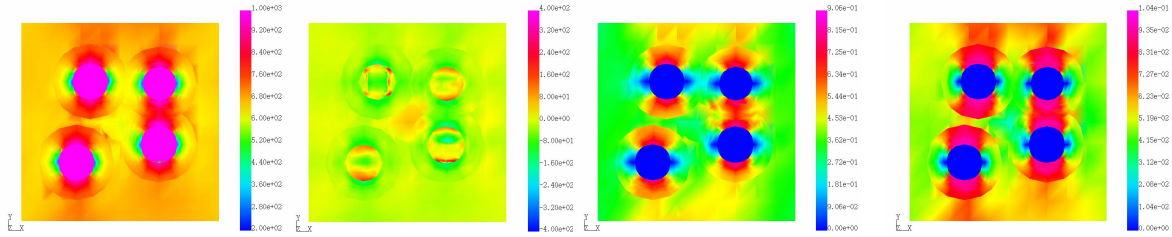

(b-1) Tensile stress (b-2) Transverse stress (b-3) Dilatational damage parameter (b-4) Deviatoric damage parameter

(b) $\bar{\varepsilon} = 0.1$

Figure 30 The distributions of the tensile and transverse stresses and the damage parameter for the case of the separate dilatational/deviatoric damage model with $\alpha = 0.1$ and without the ambient pressure (Nine randomly distributed particle model)

5.3.3 Separate dilatational/deviatoric damage material with α = 0.99 and without ambient pressure (Nine randomly distributed particle model)

The distributions of tensile and transverse stresses and the dilatational and deviatoric damage parameters are depicted in Figure 31. The concentrations of the transverse stress at the top and bottom of the particles appear more clearly than the case of $\alpha = 0.1$. The tensile stress concentrates at the top and bottom of the particles as seen in all the other cases. The values of the dilatational and deviatoric damage parameters are similar.

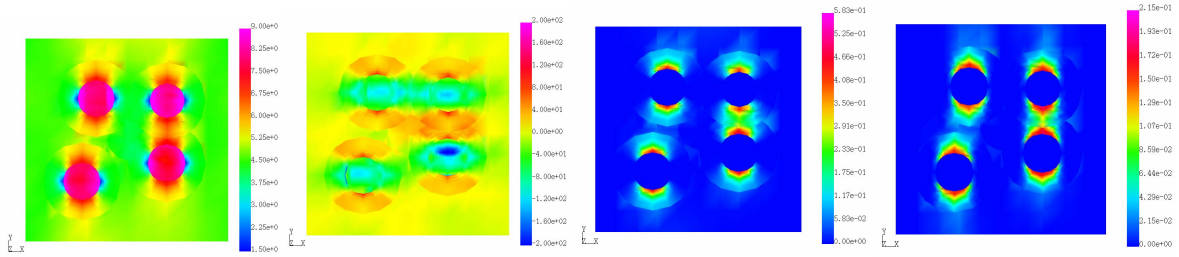

(a-1) Tensile stress (a-2) Transverse stress (a-3) Dilatational damage parameter (a-4) Deviatoric damage parameter

(a) $\bar{\varepsilon} = 0.0632$

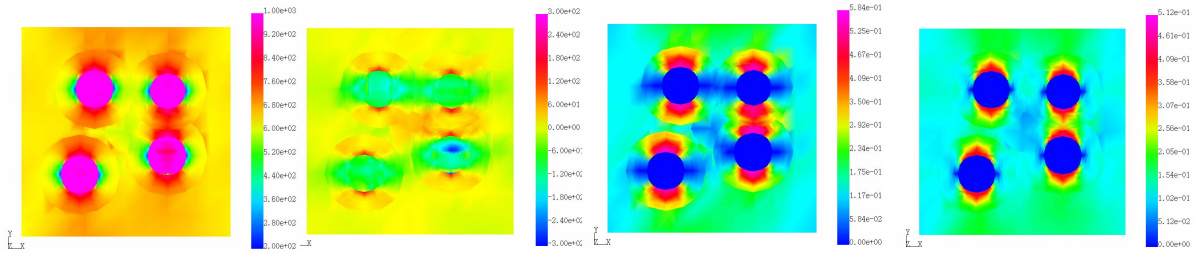

(b-1) Tensile stress (b-2) Transverse stress (b-3) Dilatational damage parameter (b-4) Deviatoric damage parameter

(b) $\bar{\varepsilon} = 0.1$

Figure 31 The distributions of the tensile and transverse stresses and the damage parameter for the case of the separate dilatational/deviatoric damage model with $\alpha = 0.99$ and without the ambient pressure (Nine randomly distributed particle model)

5.3.4 Separate dilatational/deviatoric damage material with α = 10.0 and without ambient pressure (Nine randomly distributed particle model)

The distributions of tensile and transverse stresses and the dilatational and deviatoric damage parameters are depicted in Figure 32. As seen in Figures 32 (a-2) and (b-2), the concentrations of the transverse stress at the top and bottom of the particles are clearly seen. The value of the dilatational damage parameter is much smaller than that of the deviatoric one.

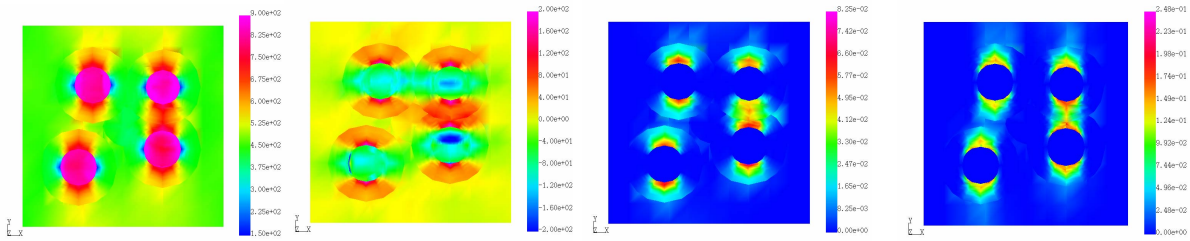

(a-1) Tensile stress (a-2) Transverse stress (a-3) Dilatational damage parameter (a-4) Deviatoric damage parameter

(a) $\bar{\varepsilon} = 0.0632$

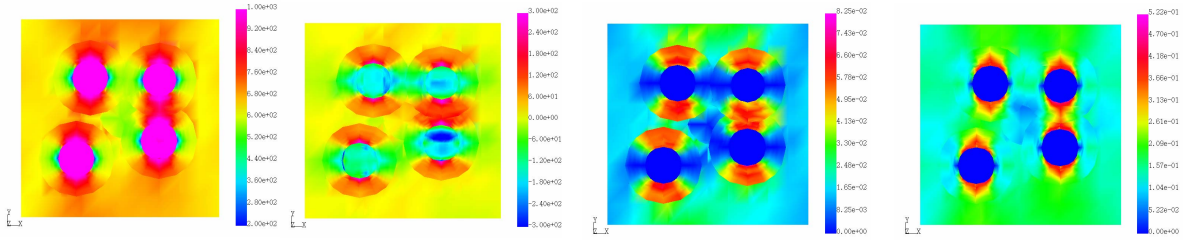

(b-1) Tensile stress (b-2) Transverse stress (b-3) Dilatational damage parameter (b-4) Deviatoric damage parameter

(b) $\bar{\varepsilon} = 0.1$

Figure 32 The distributions of the tensile and transverse stresses and the damage parameter for the case of the separate dilatational/deviatoric damage model with $\alpha = 10.0$ and without the ambient pressure (Nine randomly distributed particle model)

5.3.5 Isotropic damage material with ambient pressure (Nine randomly distributed particle model)

The distributions of tensile and transverse stresses and the damage parameter are depicted in Figure 33. As seen in the case of regularly placed four particle problem, progressive material damage at the sides of the particles are seen. They are due to negative transverse stress.

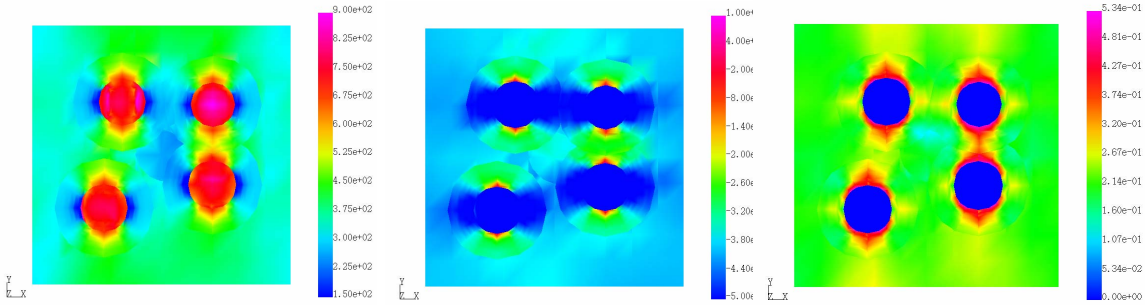

(a-1) Tensile stress (a-2) Transverse stress (a-3) Damage parameter

(a) $\bar{\varepsilon} = 0.1$

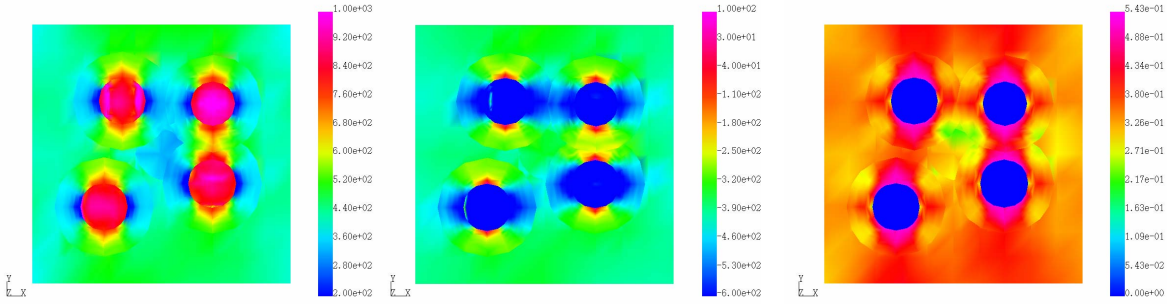

(b-1) Tensile stress (b-2) Transverse stress (b-3) Damage parameter

(b) $\bar{\varepsilon} = 0.135$

Figure 33 The distributions of the tensile and transverse stresses and the damage parameter for the case of isotropic damage with the ambient pressure (Nine randomly distributed particle model)

5.3.6 Separate dilatational/deviatoric damage material with α = 0.1 and with the ambient pressure (Nine randomly distributed particle model)

The distributions of tensile and transverse stresses and the dilatational and deviatoric damage parameters are presented in Figure 34. The distributions of the dilatational and deviatoric damage parameters are quite different from that of the damage parameter of the isotropic damage model. Also, they look differently from the case without the ambient pressure. It seems that the ambient pressure weakens the magnitude of hydrostatic stress and prevents the dilatational damage zone from enlarging in matrix material. The deviatoric damage parameter looks more uniform than the case without the ambient pressure.

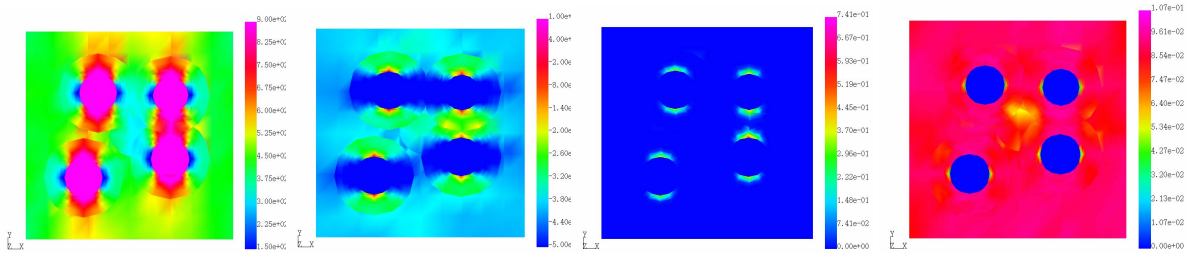

(a-1) Tensile stress (a-2) Transverse stress (a-3) Dilatational damage parameter (a-4) Deviatoric damage parameter

(a) $\bar{\varepsilon} = 0.1$

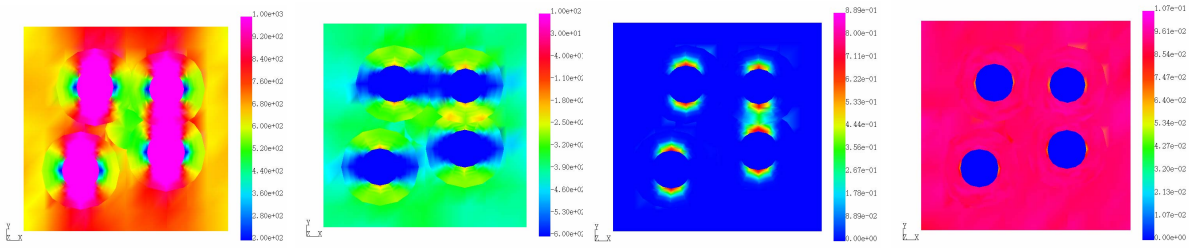

(b-1) Tensile stress (b-2) Transverse stress (b-3) Dilatational damage parameter (b-4) Deviatoric damage parameter

(b) $\bar{\varepsilon} = 0.135$

Figure 34 The distributions of the tensile and transverse stresses and the damage parameter for the case of the separate dilatational/deviatoric damage model with $\alpha = 0.1$ and with the ambient pressure (Nine randomly distributed particle model)

5.3.7 Separate dilatational/deviatoric damage material with α = 0.99 and with the ambient pressure (Nine randomly distributed particle model)

The distributions of tensile and transverse stresses and the dilatational and deviatoric damage parameters are presented in Figure 35. The levels of the dilatational damage parameter are lower than the case of $\alpha = 0.1$. In the distributions of the deviatoric damage parameter, the concentrations of the damage parameter are seen not only at the top and bottom of but also at both the sides of the particles. It seems that the compressive stress due to the ambient pressure induces the evolution of the deviatoric damage.

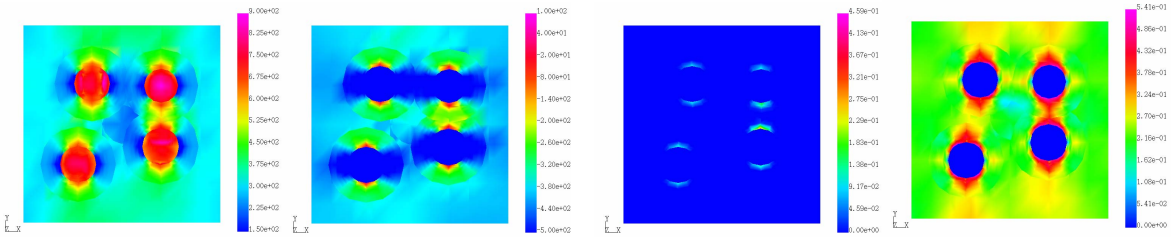

(a-1) Tensile stress (a-2) Transverse stress (a-3) Dilatational damage parameter (a-4) Deviatoric damage parameter

(a) $\bar{\varepsilon} = 0.1$

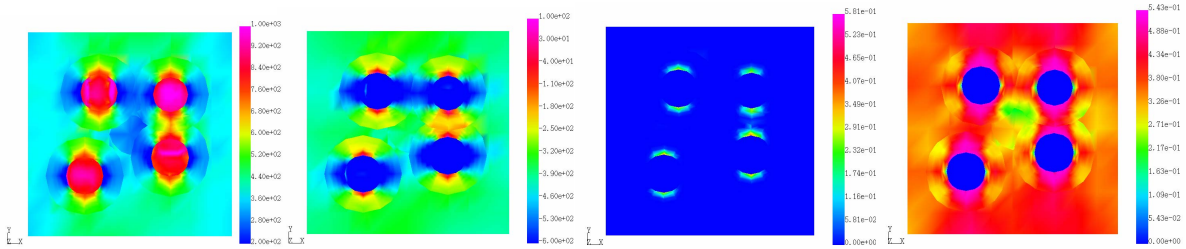

(b-1) Tensile stress (b-2) Transverse stress (b-3) Dilatational damage parameter (b-4) Deviatoric damage parameter

(b) $\bar{\varepsilon} = 0.135$

Figure 35 The distributions of the tensile and transverse stresses and the damage parameter for the case of the separate dilatational/deviatoric damage model with $\alpha = 0.99$ and with the ambient pressure (Nine randomly distributed particle model)

5.3.8 Separate dilatational/deviatoric damage material with α = 10.0 and with the ambient pressure (Nine randomly distributed particle model)

The distributions of tensile and transverse stresses and the dilatational and deviatoric damage parameters are presented in Figure 36. The major trends are the same as the case of $\alpha = 0.99$. The value of the deviatoric damage parameter is slightly larger than that of $\alpha = 0.99$. The value of the dilatational damage parameter is much smaller than those of $\alpha = 0.10$ and $\alpha = 0.99$.

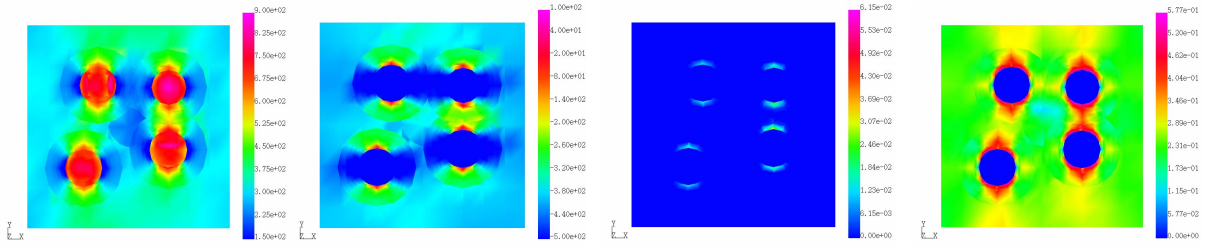

(a-1) Tensile stress (a-2) Transverse stress (a-3) Dilatational damage parameter (a-4) Deviatoric damage parameter

(a) $\bar{\varepsilon} = 0.1$

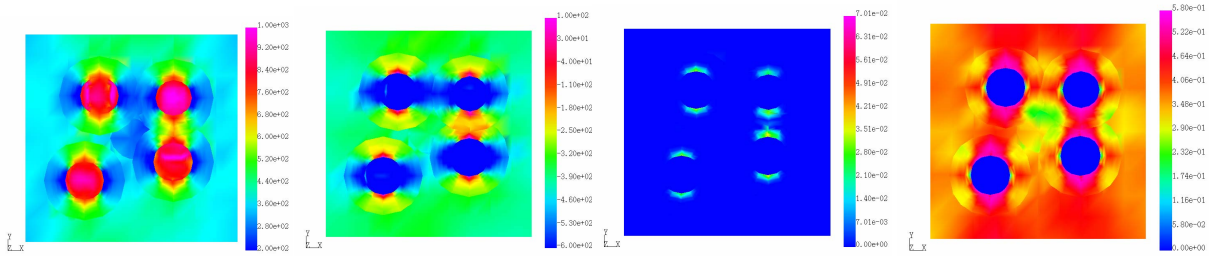

(b-1) Tensile stress (b-2) Transverse stress (b-3) Dilatational damage parameter (b-4) Deviatoric damage parameter

(b) $\bar{\varepsilon} = 0.135$

Figure 36 The distributions of the tensile and transverse stresses and the damage parameter for the case of the separate dilatational/deviatoric damage model with $\alpha = 10.0$ and with the ambient pressure (Nine randomly distributed particle model)

5.3.9 Summary: Separate dilatational/deviatoric damage material with α = 0.1, 0.99 and 10.0, and with and without the ambient pressure (Nine randomly distributed particle model)

From the sets of analyses presented in section 5.3, it is clearly seen that the major trends in the case of randomly distributed particles are the same as those in the four particle problem. However, it is seen that the damage zones connect the particles depending on their distances. The most important finding in section 5.3 is as follows. The results seem to be somewhat reasonable with all the constitutive models, i.e., the isotropic and the separate dilatational/deviatoric damage model with $\alpha = 0.1$, $\alpha = 0.99$ and $\alpha = 10.0$ when the ambient pressure is not applied. However, when the ambient pressure is applied to the block, the deviatoric damage zones develop at both the sides of the particles, where the hydrostatic stress is negative. In present study, we assume that material damage is due to the growth and nucleation of microvoids in matrix material. Such material damage is not considered to take place under negative hydrostatic stress.

Therefore, it is appropriate to use the separate dilatational/deviatoric damage constitutive model with a small number of constant α. When the constant α is small, the contribution of the deviatoric damage is small relative to that of the dilatational damage.

5.4 Material damage evolution-dewetting between the particles and matrix material (cohesive zone model)

In this section, some preliminary results are presented. Due to the softening nature of the cohesive zone model, s-FEM analyses tend to become unstable. Thus, we could not use iterative solver to solve for the system of linear simultaneous equations. Thus, we used a direct solver (skyline solver) in the analyses of section 5.4, although it is not very efficient in terms of its memory usage. It is noted that for all the other analyses, an iterative equation solver (Conjugate Gradient Method) is used. Because of this problem, we could place as many as four particles.

Since the constants δ_n, δ_t and σ_n^{MAX} in the cohesive zone model are not known, postulated values are used in the analyses. We let δ_n and δ_t be 0.01 which is much smaller than the size of the particle in out problem. σ_n^{MAX} is varied and from small to large values relative to the nonlinear stress-strain curve of Figure 16, i.e., σ_n^{MAX} =250 kPa, 500 kPa, 1000 kPa and 2000 kPa.

5.4.1 One particle model, without matrix damage (without the ambient pressure)

In this section, the results of one particle problem that is shown in Figure 37 are presented. The particle is placed in the block made of elastic material. The constants for the cohesive zone model are postulated to be:

$$\delta_n = 0.01,\quad \delta_t = 0.01,\quad \sigma_n^{MAX} \text{=250 kPa, 500 kPa, 1000 kPa or 2000 kPa} \qquad (101)$$

In Figure 38, the tensile stress distributions in the central section of the block are shown for the case of σ_n^{MAX} =250 kPa. In Figure 38 (a), the stress distribution shows stress concentrations at the top and bottom of the particle. The distribution is very similar to that without the cohesive zone model. This means that, at this step, the cohesive zone is almost rigid. In Figure 38 (b), it is seen that the stress concentrations at the top and bottom of the particle are weaker than those in Figure 37 (a). The cohesive zone opens

and the load transmitting capability of the cohesive zone starts decreasing.

In Figure 38, the distributions of the tensile stress for the case of σ_n^{MAX} =500 are shown. The trends are similar to those of σ_n^{MAX} =250. In Figures 39 and 40, the distributions are depicted for σ_n^{MAX} =1000 and σ_n^{MAX} =2000, respectively. Except for Figure 39 (b), the trends are very similar to those of σ_n^{MAX} =250 and σ_n^{MAX} =500. Due to the softening nature of the cohesive zone model, the analysis suddenly became unstable. That is why the stress distribution Figure 39 (b) looks asymmetric.

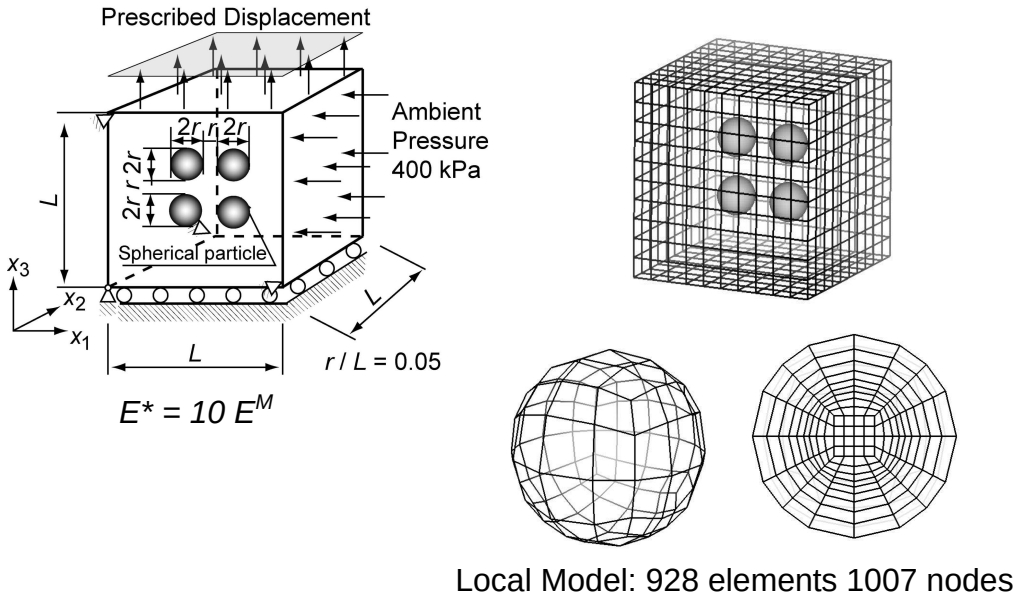

Figure 37 One particle problem with the cohesive zone model

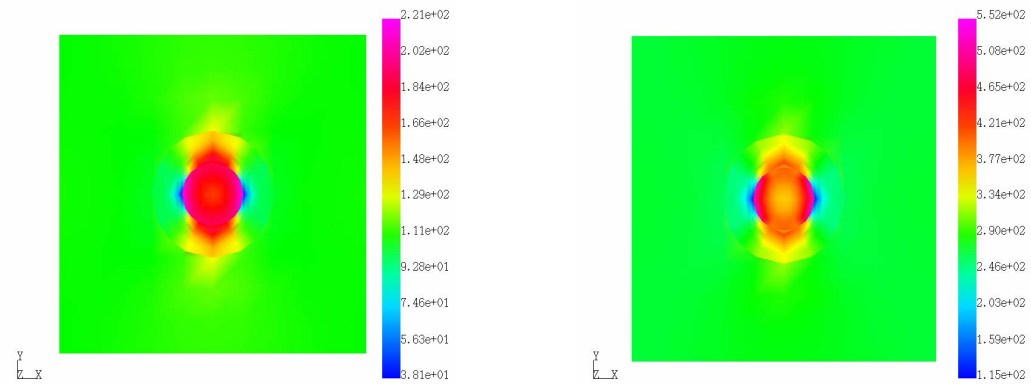

(a) Overall strain=0.015 (b) Overall strain=0.0374

Figure 37 The distributions of tensile stress for σ_n^{MAX} =250 kPa

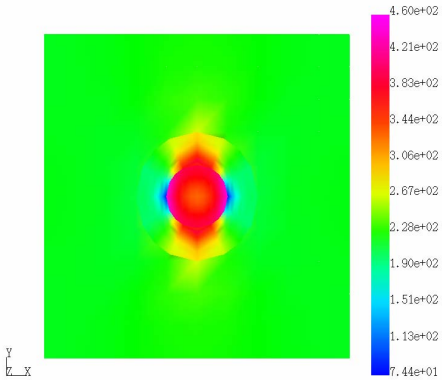

(a) Overall strain=0.03

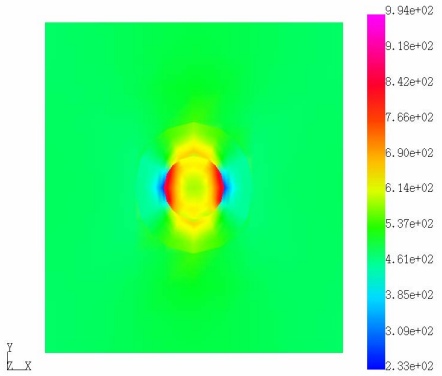

(b) Overall strain=0.0668

Figure 38 The distributions of tensile stress for σ_n^{MAX} =500 kPa

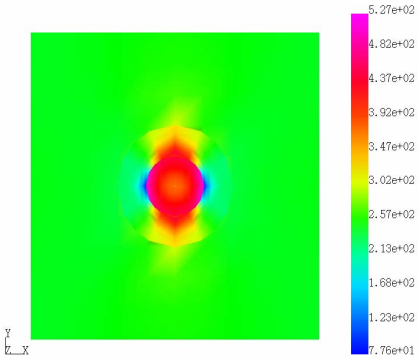

(a) Overall strain=0.03

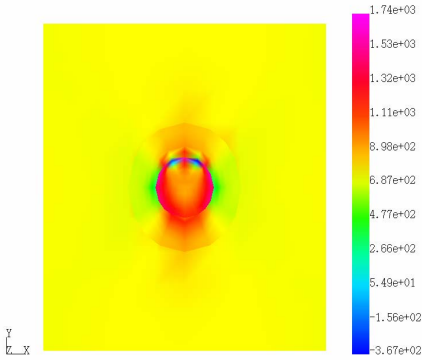

(b) Overall strain=0.1

Figure 39 The distributions of tensile stress for σ_n^{MAX} =1000 kPa

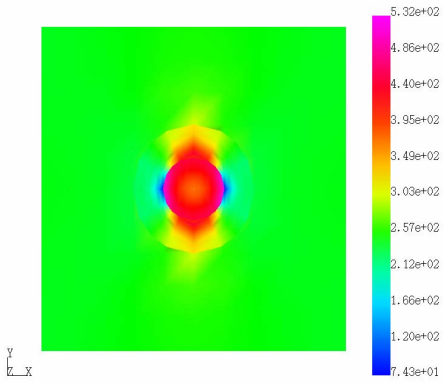

(a) Overall strain=0.03

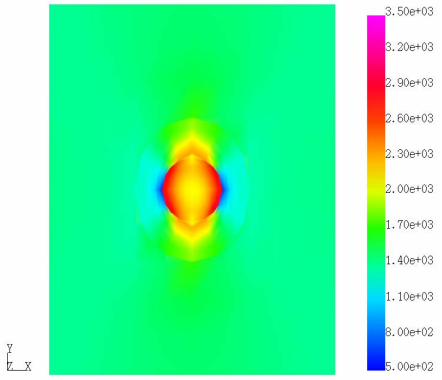

(b) Overall strain=0.195

Figure 40 The distributions of tensile stress for σ_n^{MAX} =2000 kPa

5.4.2 One particle model, with matrix damage (without the ambient pressure)

In section 5.4.2, in addition to the cohesive zone model, we assume the evolution of

material damage in matrix material. As seen in preceding sections, the separate dilatational/deviatoric damage model with a small value of constant α has been recommended to appropriately model the matrix damage due to the growth and nucleation of microvoids. Thus, in this section, α is set to be 0.1. The stress-strain curve of Figure 16 is assumed to model the behavior of matrix material. σ_n^{MAX}, a constant in the cohesive zone model is postulated to be 250 kPa, 500 kPa, 1000 kPa or 2000 kPa.

In Figure 41, the distributions of tensile stress and of the dilatational damage parameter for σ_n^{MAX} = 250 kPa are presented. It is considered that σ_n^{MAX} = 250 kPa is small compared with the level of stress-strain curve of Figure 16. According to Figure 16, the nonlinear deformation of matrix material initiates at 500 kPa. The value σ_n^{MAX} = 250 kPa is smaller than the stress at the initiation of damage. The tensile stress distribution of Figure 41 (b) indicates that the stress concentration weakens due to the opening of the cohesive zone at the top and bottom of the particle. Figure 41 (c) shows that the dilatational damage parameter is very small. Therefore, when the value of σ_n^{MAX} is small compared with that of damage initiation, the opening of cohesive zone occurs before the material damage of matrix material takes place. Therefore, the major part of the material damage is dewetting between the particle and matrix material.

In Figure 42, the distributions of tensile stress and the dilatational damage parameter are shown for σ_n^{MAX} = 500 kPa. In this case, the value of σ_n^{MAX} is comparable to the stress value at the initiation of matrix damage. In Figures 42 (a) and (c), the distributions of tensile stress and the dilatational damage parameter at overall strain 0.0441 are depicted. At this stage, the damage zone has not developed much. The tensile stress distribution is similar to that of elastic problem.

In Figures 42 (b) and (d), the distributions of tensile stress and the dilatational damage parameter are presented for overall strain being 0.0632. The stress distribution indicates that the dewetting between the particle and matrix material is taking place. Figure 42 (d) shows that the dilatational damage zones are developing at the top and bottom of the particle. In this case, both the damage modes i.e., matrix damage and dewetting between the particle and matrix take place.

In Figure 43, the distributions of tensile stress and the dilatational damage parameter are presented for σ_n^{MAX} = 1000 kPa. From the figures, it is seen that the cohesive zone does

not influence the distributions of stress and the damage parameter. The cohesive zone is so stiff that it does not open and material damage due to the dewetting does not occur. In Figure 44, the distributions are presented for σ_n^{MAX} = 2000 kPa. They are almost identical to those of σ_n^{MAX} = 1000 kPa.

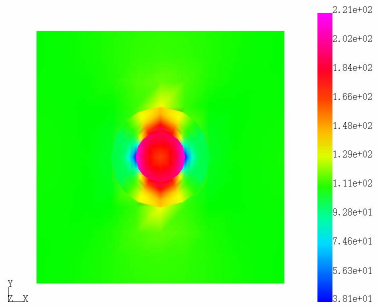

(a) Tensile stress at overall strain=0.015

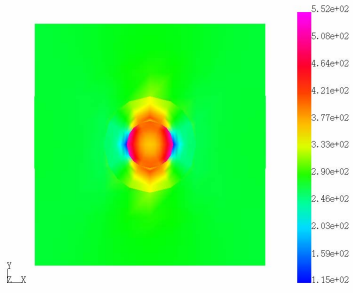

(b) Tensile stress at overall strain=0.0373

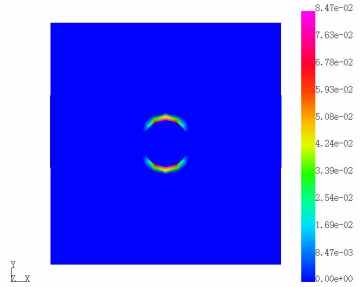

(c) Dilatational damage parameter at overall strain=0.0373

Figure 41 The distributions of tensile stress and of the dilatational damage parameter for σ_n^{MAX} =250 kPa.

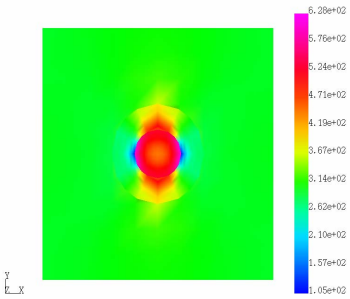

(a) Tensile stress at overall strain=0.0411

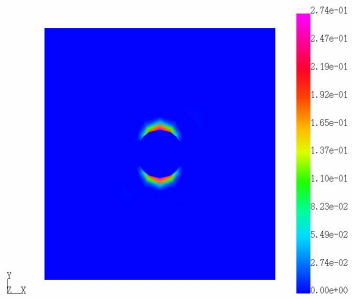

(b) Tensile stress at overall strain=0.0632

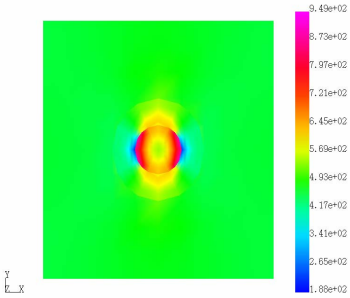

(c) Dilatational damage parameter at overall strain=0.0411

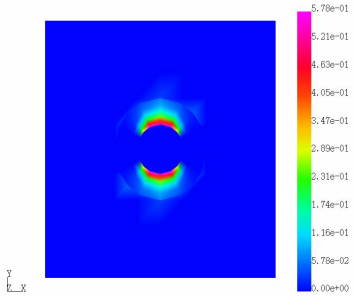

(d) Dilatational damage parameter at overall strain=0.0632

Figure 42 The distributions of tensile stress and of the dilatational damage parameter for σ_n^{MAX} =500 kPa.

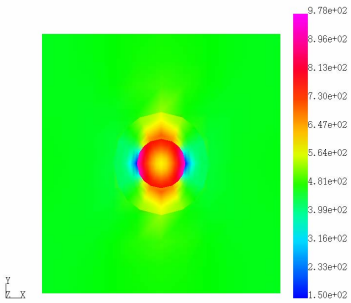

(a) Tensile stress at overall strain=0.0632

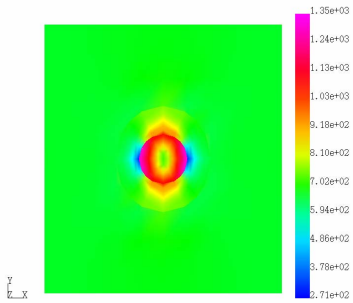

(b) Tensile stress at overall strain=0.1

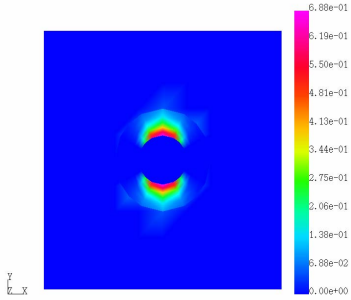

(c) Dilatational damage parameter at overall strain=0.0632

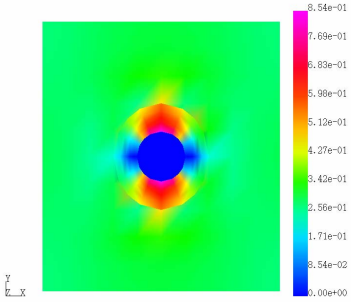

(d) Dilatational damage parameter at overall strain=0.1

Figure 43 The distributions of tensile stress and of the dilatational damage parameter for σ_n^{MAX} =1000 kPa.

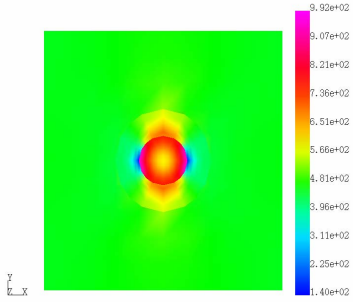

(a) Tensile stress at overall strain=0.0632

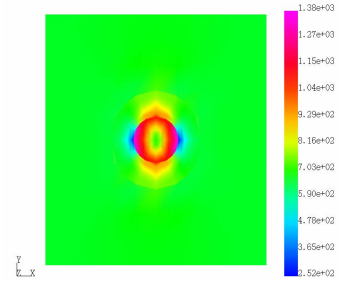

(b) Tensile stress at overall strain=0.1

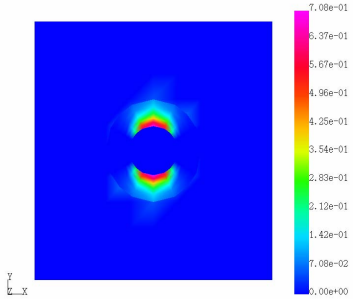

(c) Dilatational damage parameter at overall strain=0.0632

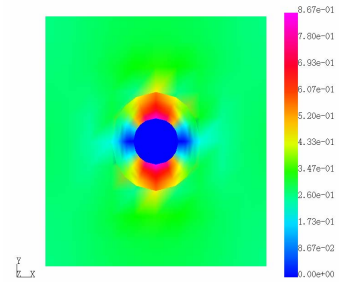

(d) Dilatational damage parameter at overall strain=0.1

Figure 44 The distributions of tensile stress and of the dilatational damage parameter for σ_n^{MAX} =2000 kPa.

5.4.3 Four particle model, with matrix damage (without the ambient pressure)

In this section, the results of analyses on the four particle model are presented. The same damage constitutive law as that is used to solve the one particle problems is adopted (the separate dilatational/deviatoric model with $\alpha = 0.1$).

In Figure 45, the distributions of tensile stress and the dilatational damage parameter for σ_n^{MAX} =250 kPa are presented. It is seen in the figures that the value of the damage parameter is small although the cohesive zones start separating and that the stress concentration at the top and bottom of the particles weakens due to the softening of the cohesive zone, i.e., dewetting.

In Figure 46, the distributions of tensile stress and he dilatational damage parameter for σ_n^{MAX} =500 kPa are depicted. In this case, the stress at the maximum stress at the cohesive zone and that at the initiation of matrix damage are comparable. It is seen in Figure 46 (b) that the stress concentration at the top and bottom of the particles weakens

due to both the damage mechanisms. The damage zones connect the particles aligned in the vertical direction, as seen in Figures 46 (c) and (d).

In Figures 47 and 48, the distributions of tensile stress and the dilatational damage parameter are presented for σ_n^{MAX} =1000 kPa and σ_n^{MAX} =2000 kPa, respectively. The distributions in Figures 47 and 48 are very similar, although the different values are given to the parameter σ_n^{MAX}. In both the cases of Figures 47 and 48, the cohesive zones do not give any influences to the deformations of the composites. The cohesive zones are stiff enough that they do not open.

As summary, we can conclude that depending on the combination of stresses at the initiation of matrix damage and at the separation of cohesive zone. In present analyses, the stress-strain curve of matrix material is postulated to be what was given in Kwan and Liu [10] and the parameter σ_n^{MAX} of cohesive zone model that governs the stress at the separation of cohesive zone is varied. When σ_n^{MAX} is set to be 250 kPa, the stress at the separation of cohesive zone is smaller than that at the initiation of matrix damage. In such a case, interface separation at the cohesive zone is the major damage mechanism of the composite. When σ_n^{MAX} is 500 kPa, the stress at the separation of cohesive zone is comparable to that at the progress of matrix damage. Both the mechanisms of material damage take place. When σ_n^{MAX} is 1000 kPa or 2000 kPa, the interface separation at the cohesive zone do not occur at all. The matrix damage is the major damage mechanism.

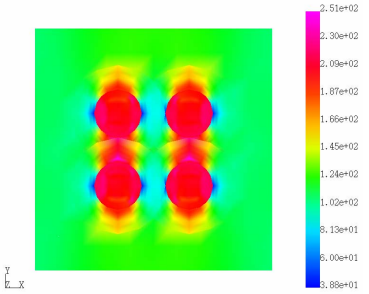

(a) Tensile stress at overall strain=0.015

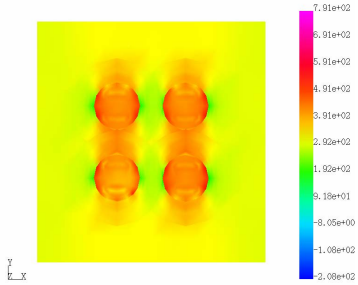

(b) Tensile stress at overall strain=0.0411

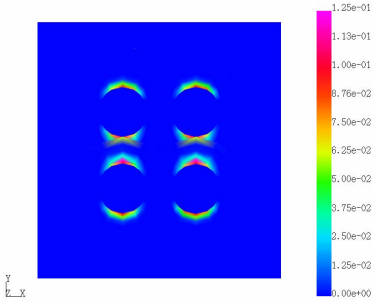

(c) Dilatational damage parameter at overall strain=0.0411

Figure 45 The distributions of tensile stress and of the dilatational damage parameter for σ_n^{MAX} =250 kPa (four-particle problem).

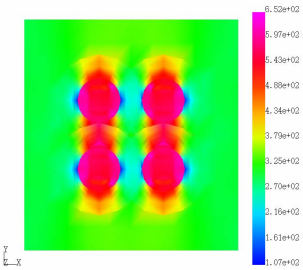

(a) Tensile stress at overall strain=0.0411

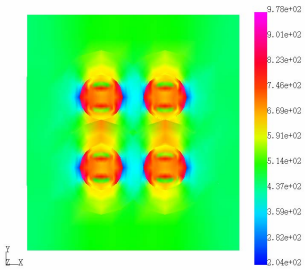

(b) Tensile stress at overall strain=0.0632

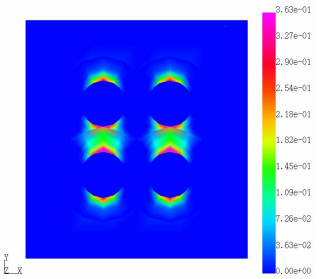

(c) Dilatational damage parameter at overall strain=0.04112

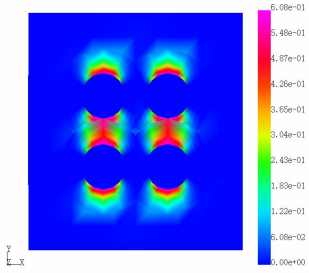

(d) Dilatational damage parameter at overall strain=0.0632

Figure 46 The distributions of tensile stress and of the dilatational damage parameter for σ_n^{MAX} =500 kPa (four-particle problem)

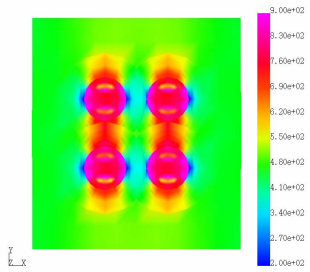

(a) Tensile stress at overall strain=0.0632

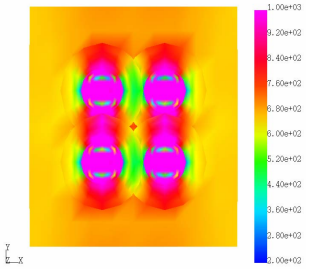

(b) Tensile stress at overall strain=0.1

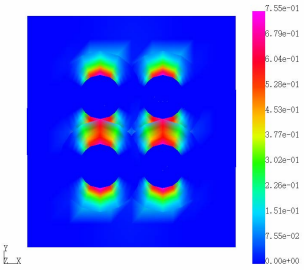

(c) Dilatational damage parameter at overall strain=0.0632

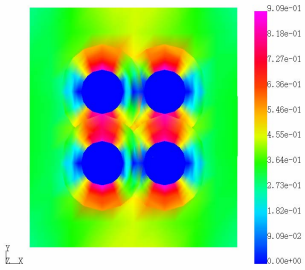

(d) Dilatational damage parameter at overall strain=0.1

Figure 47 The distributions of tensile stress and of the dilatational damage parameter for σ_n^{MAX} =1000 kPa (four-particle problem)

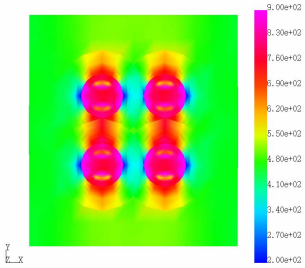

(a) Tensile stress at overall strain=0.0632

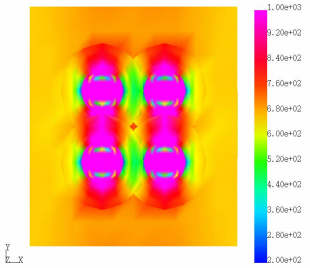

(b) Tensile stress at overall strain=0.1

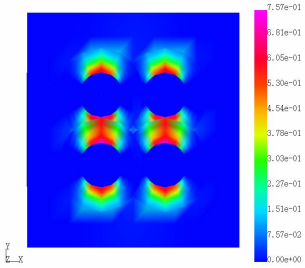

(c) Dilatational damage parameter at overall strain=0.0632

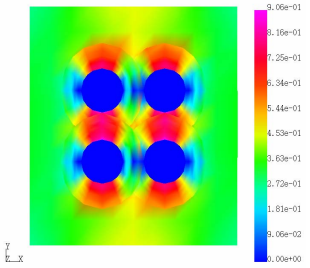

(d) Dilatational damage parameter at overall strain=0.1

Figure 47 The distributions of tensile stress and of the dilatational damage parameter for σ_n^{MAX} =2000 kPa (four-particle problem)

6. Conclusions

In this investigation, the deformation and damage mechanisms of particulate composite material are investigated. To do so, we adopted the s-version Finite Element Method (s-FEM). By using the s-FEM, the finite element models for the structure as whole and for a particle and its vicinity are built separately and are superposed each other. They are called the global and the local finite element models. Once the global model and the local model are built, they are superposed in any fashion as long as the region of the local model is included in that of the global model. The local model can be superposed on the global model repeatedly and they can also overlap each other. Thus, as seen in this report, without building new finite element models, various particle arrangements can be modeled without creating any new finite element models.

In this research, continuum damage constitutive models are adopted. They are based on Simo and Ju [6]. To account for the contributions of the hydrostatic and deviatoric stresses independently, the separate dilatational/deviatoric damage constitutive model was adopted. By adjusting a constant in the model, we can model various combinations of the contributions from the hydrostatic and deviatoric stresses. For example, when the constant α is set to zero, purely dilatational damage solid is modeled. When $\alpha = 1$, the behavior of the solid is similar to that of isotropic damage material. $\alpha \to \infty$ results in a deviatoric damage material.

Cohesive zone model is implemented in the s-FEM computer program to account for dewetting between the particles and matrix material. Only the local finite element model contains the cohesive zone as the global model does not account for the details of the structure such as the particles. The cohesive zone, when it separates, has a softening behavior. The iterative equation solver (Conjugate Gradient Method) that is adopted in the program can not handle the softening behavior. Thus, a direct solver (Skyline method) was used to solve the problems. The direct solver requires much larger memory space than the iterative one does. Therefore, it was difficult to place many particles. At most, we could place four particles.

The results presented in this report revealed that the use of isotropic damage model is not appropriate since the material damage may progress under a negative hydrostatic stress. The use of the separate dilatational/deviatoric damage model is recommended with the hydrostatic stress having the major contribution. The evolutions of progressive

damage zones are presented. When the particles are aligned in the loading direction, the damage zones connect the particles. Due to the strong constraint from the particle, damage zones do not develop at the sides of the particle.

Dewetting between the particles and matrix material is seen to initiate at the top and the bottom of the particles. Dewetting does not occure at the sides of the particles. Depending on the strength of bond between the particles and matrix material, dominant damage mechanism changes. When the bond is very strong, i.e., the value of constant σ^{Max} is large, only the matrix damage occurs. When the bond is very weak, i.e., σ^{Max} is small, dewetting is the dominant damage mechanism. When the strength of the bond is comparable to the stress at the initiation of matrix damage, both the damage mechanisms take place.

Although s-FEM computer code has been developed for the damage analyses, the material constants that were adopted in the analyses are postulated ones. However, some characteristic behavior of particulate composite materials with progressive damage has been revealed.

In summary, during present research, the followings have been accomplished.

1) The separate dilatational/deviatoric damage constitutive model was proposed along with a method to extract its material parameters from one-dimensional stress-strain curve. The damage model was implemented in the s-FEM computer program,
2) S-FEM formulation with the cohesive zone model has been proposed and has been implemented in the s-FEM program.
3) S-FEM analyses on particulate composite materials, with assuming the matrix damage and dewetting between the particles and matrix material, has been carried out. Some characteristic behavior of damages in the particulate composite materials has been revealed.

References

(1) J. Fish
The s-Version Finite Element Method, *Computers & Structures*, Vol. 43, pp. 539-347, 1992.
(2) K.-J. Bathe
Finite element procedures, Prentice-Hall, Inc., Upper Saddle River, NY, 1996.
(3) T. J. R. Hughes
The finite element method –Linear static and dynamic finite element analysis, Prentice-Hall, Englewood Cliffs, N.J., 1987.
(4) I. S. Sokolnikoff
Mathematical theory of elasticity second edition, McGraw-Hill, New York, 1996.
(5) H. Okada, C.T. Liu, T. Ninomiya, Y. Fukui, N. Kumazawa
Analysis of particulate composite materials using an element overlay technique. *Computer Modeling in Engineering & Sciences*. Vol. 6, pp. 333-347, 2004.
(6) J. C. Simo and J.W. Ju
Strain- and Stress Based Continuum Damage Models-I. Formulation, *Int. J. Solids Structures*, Vol. 23, pp. 821-840, 1987.
(7) J. C. Simo and J.W. Ju
Strain- and Stress Based Continuum Damage Models-II. Computational Aspects, *Int. J. Solids Structures*, Vol. 23, pp. 841-869, 1987.
(8) N. Chandra, H. Li, C. Shet and H. Ghonem
Some Issues in the Application of Cohesive Zone Models, Int. J. Solids Structures, Vol. 39, pp. 2827-2855.
(9) J. W. Foulk, D. H. Allen and K. L. E. Helms
Formulation of a Three-Dimensional Cohesive Zone Model for Application to a Finite Element Algorithm, Comput. Methods Appl. Mech. Engrg, Vol. 183, pp. 51-66, 2000.
(10) Y. W. Kwon and C. T. Liu
Effect of Particle Distribution in Initial Cracks Forming from Notch Tips of Composites with Hard Particles Embedded in a Soft Matrix, *Composites Part B*, Vol. 32, pp. 199-208, 2001.

Publications

S. Tanaka, H. Okada, Y. Watanabe, T. Wakatsuki
Applications of s-FEM to the problems of composite materials with initial strain-like

terms, submitted to International Journal for Multiscale Computational Engineering, 2005 (accepted for the publication).

S. Tanaka, H. Okada, Y. Watanabe
Application of s-version FEM to the mesoscopic analysis of Wavy Shape Memory Fiber/Plaster Smart Composite, WCCM (International Congress on Computational Mechanics) IV, CD-ROM, 2004.

H. Okada, C.T. Liu and S. Tanaka
Analysis of Damage Evolution of Particulate Composite Material using the s-version FEM, *Proceedings of* International Conference on Computational & Experimental Engineering and Sciences 2005 (ICCES'05) (Edt. by S.M. Sivakumar, M. Meher Prasad, B. Dattaguru, S. Narayanan, A.M. Rajendran, S.N. Atluri), CD-ROM, 2005.

H. Okada and Y. Kamimaru
BEM Analysis on Crack Tip Deformation Field of Rubber-Modified Epoxy Resin, Adhesive Layer *Proceedings of* International Conference on Computational & Experimental Engineering and Sciences 2005 (ICCES'05) (Edt. by S.M. Sivakumar, M. Meher Prasad, B. Dattaguru, S. Narayanan, A.M. Rajendran, S.N. Atluri), CD-ROM, 2005.

H. Okada, S. Tanaka, Y. Fukui and N. Kumazawa
Analyses of progressive damage and fracture of particulate composite materials using S-FEM technique, to be presented at ECF16 (16th European Conference on Fracture), 2006.

Acknowledgements

The investigator of present research would like to express sincere thanks to the support from Asian Office of Aerospace Research and Development (AOARD). The sincere gratitude is extended to Drs. J.P.Singh and K. Goretta for his encouragements during course of study and to Dr. C.T. Liu (formerly with Air Force Research Laboratory) for his kind guidance and technical support. Without their support, it was not possible to perform present investigation.

Former and current graduate students at the Graduate School of Science and

Engineering of Kagoshima University put a lot of efforts in developing computer codes, in performing computation and in visualizing the results. Many thanks are extended to them (Mrs. Y. Sakasegawa, T. Ninomiya, Y. Kamimaru, T. Kamibeppu, K. Sanada, K. Oya and S. Tanaka).